Department of Physics and Astronomy
Heidelberg University

Master Thesis in Physics
submitted by

**Jelte Jan Luca Duchêne**

born in Flensburg, Germany
2024

# Designed Boundaries for Phonon-Based Quantum Simulations

This Master Thesis has been carried out by
Jelte Jan Luca Duchêne
at the Kirchhoff-Institute of Physics
under the supervison of
Prof. Dr. Markus K. Oberthaler

# Zusammenfassung

## Designte Ränder für phononenbasierte Quantensimulationen

In analogen Quantensimulatoren, die auf räumlich kontinuierlichen kalten Atomwolken basieren, sind Endlichkeits- und Randeffekte oft erheblich. Theoretische Modelle nehmen häufig unendlich ausgedehnte Systeme an, was Vergleiche mit Experimenten endlicher Größe erschwert. In dieser Arbeit verwenden wir einen Quantensimulator, der auf phononischen Anregungen in einem quasi-zweidimensionalen Bose-Einstein-Kondensat von Kalium-39-Atomen basiert, um zu untersuchen, wie das sogenannte "slanted box" (slox)-Potenzial die kohärente Reflexion von Phononen unterdrückt und gleichzeitig die Atome einschließt. Dieses Potenzial ist im Zentrum flach und steigt an den Rändern linear an. Mit diesem absorbierenden Verhalten des slox können wir effektiv ein unendlich ausgedehntes System nachbilden. In dieser Arbeit werden Wellenpaketdynamiken in 2D-Experimenten mit 1D-Simulationen verglichen. Zusätzlich wird der Einfluss verschiedener Ränder auf die Entstehung und Stabilität von spontan gebildeten Dichtemustern in einer wechselwirkungsgetriebenen Situation untersucht. Wir zeigen, dass räumliches Rauschen im Lichtpotenzial entscheidend dafür ist, diese Reflexionen effizient zu unterdrücken. Außerdem wurde im Rahmen dieser Arbeit ein neuer Laser für die D1- und D2-Linien von Kalium, der Telekommunikationstechnologie bei ∼1540 nm und Frequenzverdopplung nutzt, aufgebaut und charakterisiert.

# Abstract

## Designed Boundaries for Phonon-Based Quantum Simulations

In analogue quantum simulators based on spatially continuous cold atom clouds, finite size and boundary effects are often substantial. Theoretical models often assume an infinitely extended systems, which makes comparisons with finite-size experiments challenging. In this thesis, we use a quantum simulator based on phononic excitations in a quasi-two-dimensional Bose-Einstein condensate of potassium-39 atoms to investigate how the so-called slanted box (slox) potential suppresses the coherent reflection of phonons while still confining the atoms. This potential is flat in the center and increases linearly at the edges. With this absorptive behavior of the slox, we can effectively mimic an infinitely extended system. In this thesis wavepacket dynamics in 2D experiments are compared to 1D simulations. Additionally, the influence of various boundaries on the emergence and stability of spontaneously formed density patterns in an interaction-driven situation is investigated. We show that spatial noise in the light potential is crucial for efficiently suppressing these reflections. Additionally, a new laser for the potassium D1- and D2-lines, using telecommunication technology at ∼1540 nm and second harmonic generation, was built and characterized in the scope of this thesis.

# Contents

**1. Introduction** **5**

**2. Theoretical and Experimental Fundamentals** **7**
2.1. Bose-Einstein Condensate . . . . . 7
2.2. Thomas-Fermi Approximation . . . . . 8
2.3. Quasi Two-Dimensional Bose-Einstein Condensate . . . . . 9
2.4. Bogoliubov Approximation . . . . . 9
2.5. Numerical Simulation Methods . . . . . 11
2.6. Dipole Potential . . . . . 13
2.7. Experimental Setup: Cooling, Trapping and Imaging . . . . . 13

**3. Wavepacket Analysis** **16**
3.1. Experimental Wavepacket Preparation and Propagation in Slox Potential with Different Slopes . . . . . 16
3.2. Wavepacket Preparation and Propagation in 1D-GPE Simulation . . . . 19
3.2.1. Wavepacket Propagation in Slox Potential with Various Slopes . . 20
3.2.2. Propagation of Wavepackets with Various Widths . . . . . 21
3.2.3. Propagation of Wavepackets with Various Amplitudes . . . . . 22
3.2.4. Wavepacket Simulation in 2D Assuming Radial Symmetric Solution 24
3.2.5. Truncated Wigner Approximation . . . . . 25
3.3. Accounting for Noise in the Light Potential . . . . . 26
3.3.1. An Indicator for Reflectivity . . . . . 28
3.4. Artificial Noise in the Trapping Potential . . . . . 30
3.5. Hyperbolic Geometry for Absorptive Boundaries . . . . . 31

**4. Spontaneous Pattern Formation Analysis** **33**
4.1. Quantifying Occupations and Correlations of the Pattern . . . . . 33
4.2. Effects of Different Potentials on Pattern Formation . . . . . 36
4.3. Pattern Formation for Different Noise Scales on the Potential . . . . . 38

**5. Conclusion and Outlook** **41**

**A. New Calibration Method for Light Potential Optimization Algorithm** **47**
A.1. Is a Linear Transformation Enough? . . . . . 49
A.2. Affine Transformation . . . . . 49

**B. New Laser for the Potassium D1- and D2-Lines** **52**
B.1. The Main Components: Seed, Amplifier, SHG Crystal . . . . . 53
B.2. SHG Setup . . . . . 54
B.3. Frequency Stabilization on Potassium Absorption Lines . . . . . 55
B.4. Current Status and Outlook . . . . . 58

B.5. List of Components for Laser Setup . . . . . 59
B.6. Wiring Diagram for Laser Setup . . . . . 60
B.7. Python Script for Communication with Seed Laser . . . . . 60

# List of Figures

2.1. Thomas-Fermi Profile . . . 9
2.2. Overview of the Experimental Setup . . . 14
3.1. Experimental Wavepacket Preparation and Propagation . . . 17
3.2. Experimental Wavepacket Propagation in Slox Potentials with Different Slope . . . 18
3.3. Wavepacket Preparation and Propagation in 1D-GPE Simulation . . . 20
3.4. Wavepacket Propagation in Slox Potential with Various Slopes . . . 21
3.5. Propagation of Wavepackets with Various Widths . . . 21
3.6. Propagation of Wavepackets with Various Amplitudes . . . 22
3.7. Local Density Approximation vs. Extracted Speed . . . 23
3.8. Wavepacket Simulation in 2D Assuming Radial Symmetric Solution . . . 25
3.9. Truncated Wigner Approximation . . . 26
3.10. Wavepacket Propagation in Rough and Smooth Slox Potential: Simulation and Experiment Comparison. . . . 27
3.11. Standard Deviation of the Density Difference as Indicator for Reflectivity 28
3.12. Experimental Wavepacket Propagation in Optimized Slox Potentials with Different Slope . . . 29
3.13. Atom Densities and Wavepacket Propagation for Different Noise Scales on the Potential . . . 30
3.14. Wavepacket Dynamics in a Hyperbolic Geometry . . . 32
4.1. Spontaneous Pattern Formation . . . 34
4.2. Quantifying Occupation and Correlation of the Pattern . . . 35
4.3. Effects of Different Potentials on Pattern Formation . . . 37
4.4. Pattern Formation for Different Noise Scales on the Potential . . . 39
A.1. Previous DMD Calibration . . . 47
A.2. Schematic Illustration of Affine Transformation Effects . . . 48
A.3. Rings in the Atom Plane . . . 49
A.4. Affine Transformation for DMD Calibration . . . 50
B.1. Level Scheme of $^{39}$K and $^{41}$K . . . 53
B.2. Schematics of the Laser Setup . . . 54
B.3. Pump and SHG Power . . . 55
B.4. Doppler-free Absorption Spectrum . . . 56
B.5. Control Signal for Frequency-Locking . . . 57
B.6. Wiring Diagram for Control Signal Processing . . . 60

# 1. Introduction

Analogue quantum simulation has become an important tool in modern research. The concept was first introduced by Feynman in 1982, who argued that quantum systems should be simulated using other inherently quantum systems rather than classical computers [1]. The idea behind quantum simulation is as follows: given a system A that is impractical to probe directly - for instance, because it is experimentally inaccessible - but whose Hamiltonian is known, it can be simulated using a system B with high experimental control, provided the Hamiltonian of system B can be mapped onto that of system A.

In recent years, experimental platforms, especially those using ultracold atoms, have become crucial for quantum simulation. This is due to their excellent experimental control over the Hamiltonians governing the systems. Examples include simulation with Fermi gases [2, 3], with quantum gas microscopes [4, 5], quantum computing with Rydberg atoms [6, 7], and many more exciting developments in this rapidly growing field. Comparisons between theoretical models and experimental results are crucial to progress in any field. However, many theoretical models assume infinite extension or periodic boundary conditions, making simulations with finite-size experiments challenging.

In our group, we use a quantum simulator based on phononic excitations in a quasi-two-dimensional Bose-Einstein condensate of potassium-39 atoms (the BECK experiment). This setup has been used to explore phenomena such particle production in the early universe [8, 9], wave propagation in curved spacetime [8], the emergence and stability of a pattern with supersolid sound modes [10, 11] and implementing a non-linear block of machine learning [12]. This is made possible by precise experimental control of the interaction strength via a so-called Feshbach resonance using magnetic fields and of the external potential using a digital micromirror device (DMD) to project various dipole potentials onto the atoms.

We use a so-called slanted box (slox) potential to effectively mimic infinite system sizes by suppressing coherent reflections at the boundary while conserving the atom number. This potential is flat in the center and has linearly rising slopes at the edges and experimentally achieved by using the DMD. This thesis aims to understand why the slox potential suppresses coherent phonon reflections. For that, we study wavepacket dynamics in 2D experiments and 1D simulations as well as the influence of parameters of the slox potential on the emergence and stability of spontaneously formed density patterns in an interaction-driven situation.

The thesis is outlined as follows: In Section 2, the theoretical and experimental fundamentals necessary to understand and interpret the content of this thesis are presented. Afterwards, in Section 3, results from wavepacket analysis in the 2D experiment with various boundary conditions are discussed, and the underlying mechanism for the sup-

pression of coherent reflections in the slox potential is investigated using 1D simulations. In Section 4, the effects of different boundary conditions on the spontaneous emergence of square patterns when modulating the interaction strength are presented. Finally, in Section 5, the conclusions from all investigations are summarized, and an outlook for further research and potential applications of the slox potential is provided. In Appendix A, a new calibration method for the iterative feedback algorithm that is used to optimize the light potential is presented. Additionally, the new laser system for the potassium D1- and D2-lines is described and characterized in Appendix B.

# 2. Theoretical and Experimental Fundamentals

In this Section, the theoretical and experimental fundamentals, necessary to understand and interpret the content of this thesis are outlined. In Section 2.1, the equation describing the ground state of a Bose-Einstein condensate (BEC), the Gross-Pitaevskii Equation (GPE), will be derived by considering a bosonic gas in the ultra-cold, dilute, and weakly interacting regime. Section 2.2 covers the Thomas-Fermi approximation, which provides a good initial estimation for the ground state of a BEC with repulsive interactions in an arbitrary external potential. The treatment of tight confinement in one spatial direction is explained in Section 2.3. In Section 2.4 the derivation for the dynamics of small density excitations on the background BEC, known as Bogoliubov phonons, is provided. A method for numerically simulating the GPE is presented in Section 2.5. In Section 2.6, the dipole potential, used for conservative traps, is explained. Finally, Section 2.7 describes the BECK experiment, which was used to produce all experimental data. The structure of the theoretical fundamentals are based on the lectures from Mikhail Baranov and Jean-Philippe Brantut, held at the École de Physique in Les Houches 2024.

## 2.1. Bose-Einstein Condensate

Consider $N$ bosonic particles in a volume $\mathcal{V}$, such that the density $n = N/\mathcal{V}$ is low enough that interactions between more than two particles can be neglected. The Hamiltonian such a system, in term of bosonic field operators $\hat{\Psi}$, is [13]

$$\begin{aligned}\hat{H} = \int \left( -\frac{\hbar^2}{2m} \nabla\hat{\Psi}^\dagger(\vec{x}) \nabla\hat{\Psi}(\vec{x}) + \hat{\Psi}^\dagger(\vec{x}) V(\vec{x}) \hat{\Psi}(\vec{x}) \right) d\vec{x} \\ + \int \hat{\Psi}^\dagger(\vec{x}\,') \hat{\Psi}^\dagger(\vec{x}) \, V_{\text{int}}(\vec{x}\,' - \vec{x}) \hat{\Psi}(\vec{x}\,') \, \hat{\Psi}(\vec{x}) \, d\vec{x} \, d\vec{x}\,',\end{aligned} \tag{1}$$

where $m$ is the atomic mass, $\hbar$ the reduced Planck constant, $V$ an external potential, and $V_{\text{int}}$ the two-particle interaction potential. In second quantization, the field operator can be written in terms of single-particle wavefunctions $\phi_{\vec{p}}\,(\vec{x})$,

$$\hat{\psi}(\vec{x}) = \frac{1}{\sqrt{\mathcal{V}}} \sum_{\vec{p}} \, \hat{a}_{\vec{p}} \, \phi_{\vec{p}}\,(\vec{x}), \tag{2}$$

where $\hat{a}_{\vec{p}}$ is the operator that annihilates a particle with momentum $\vec{p}$. The operators $\hat{a}_{\vec{p}}$ and $\hat{a}^\dagger_{\vec{p}}$ fulfill the bosonic commutation relation $[\hat{a}_{\vec{p}}, \hat{a}^\dagger_{\vec{p}\,'}] = \delta_{\vec{p}\,',\vec{p}}$. Considering the regime of weakly interacting, low-density, and low-temperature particles, means the two-particle interaction length $r_0$ is much smaller than the interparticle distance $\sim n^{-1/3}$, which is itself smaller than the de Broglie wavelength $\sim \hbar/\sqrt{mk_BT}$:

$$r_0 \ll n^{-1/3} < \frac{\hbar}{\sqrt{mk_BT}}, \tag{3}$$

where $k_B$ is the Boltzmann constant and $T$ the temperature. In this regime, only s-wave scattering is relevant for two-particle collisions, and hence the interaction potential can be replaced by a single interaction strength $g = \frac{4\pi\hbar^2}{m} a_s$, where $a_s$ is the scattering length. For a Bosonic gas in thermal equilibrium, the distribution of $N$ particles over the momentum modes with $p = |\vec{p}|$ is given by [13]

$$N = \sum_p N_p = \sum_p \left\langle a_p^\dagger a_p \right\rangle = \sum_p \frac{1}{\exp\left(\hbar^2 p^2/2m - \mu_0\right)/k_B T - 1}, \tag{4}$$

where $\mu_0$ is the chemical potential of the reservoir, with which the Bosons are in thermal equilibrium. Low temperatures imply that $N_0 = \langle \hat{a}_0^\dagger \hat{a}_0 \rangle$ is much larger than 1 resulting in the state being macroscopically occupied, with $N_0 \approx N$. While the state $N_{p\neq 0}$ is also largely occupied, it will never be of the order $\mathcal{O}(N)$, at low temperatures. As the commutator for $\hat{a}_0$ and $\hat{a}_0^\dagger$ is of order $\mathcal{O}(1)$ and therefore much smaller than $\sqrt{N_0}$, this allows us to replace $\hat{a}_0$ by a complex number and replace $\hat{a}_0 \phi_0(\vec{x})$ by the so-called mean field or condensed fraction $\Psi$. The higher momenta are captured by small perturbations $\delta\Psi$ and their dynamics will be explained in Section 2.4. The equation of motion for the mean field, in the Heisenberg picture, is derived using Equation (1) and amounts to

$$i\hbar \partial_t \Psi = \left( -\frac{\hbar^2}{2m} \nabla^2 + V(\vec{x}) + g|\Psi|^2 \right) \Psi. \tag{5}$$

This is known as the Gross-Pitaevskii Equation (GPE), derived by Eugene Gross [14] and Lev Pitaevskii [15] in 1961. The general solution takes the form

$$\Psi(\vec{x}, t) = \sqrt{n(\vec{x})} \exp\left(-i\mu_0 t/\hbar\right), \tag{6}$$

where $\mu_0$ is the chemical potential and $n = \Psi^* \Psi$ is the atom density.

## 2.2. Thomas-Fermi Approximation

For a dense cloud in a large trapping potential, the kinetic term can be neglected. In this so-called Thomas-Fermi approximation, plugging the ansatz (6) into the GPE yields

$$n(\vec{x}) = \frac{\mu_0 - V(\vec{x})}{g}. \tag{7}$$

Within this approximation, the atomic density is inversely proportional to the potential, and the potential is filled up to the chemical potential $\mu_0$, as schematically illustrated in Figure 2.1. The approximation fails where the spatial derivative in the density cannot be neglected, i.e., at the edges of the condensate and at discontinuities in the potentials. This is captured by the minimal characteristic length required for a local perturbation, called the healing length $\xi = \frac{\hbar}{\sqrt{mng}}$.

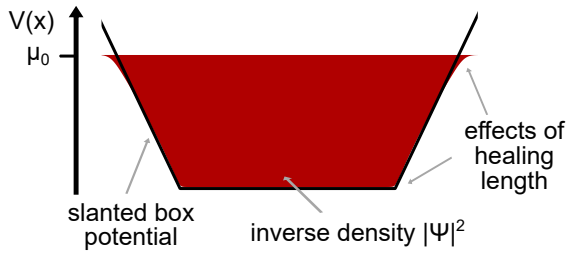



Figure 2.1: **Thomas-Fermi Profile for a Slanted Box Potential.** Within the Thomas-Fermi approximation, the atomic density of the ground state is given the balance of the external potential $V(\vec{x})$ and the chemical potential $\mu_0$. At the edges of the condensate or at discontinuities of the potentials the kinetic term, i.e the spatial derivative of the atom density, cannot be neglected. Deviations from the Thomas-Fermi approximation are captured by the characteristic length for a local perturbation, the healing length $\xi = \frac{\hbar}{\sqrt{mng}}$.

## 2.3. Quasi Two-Dimensional Bose-Einstein Condensate

Confining the BEC tightly in one direction restricts the dynamics to the other two dimensions. The scattering length $a_s$ remains a good approximation in the two-body interaction, as long as the length of the atom-atom interaction is still small compared to the expansion in the $z$-direction. For a tight harmonic trap in the $z$-direction, $V(z) = \frac{1}{2}m\omega_z^2 z^2$, the GPE can be solved by factorizing the wavefunction $\Psi(x, y, z) = \Psi_{2D}(x, y) \cdot \Psi_z(z)$. Here $\Psi_z(z)$ is the ground state when neglecting the interaction term

$$\Psi_z(z) = \frac{1}{(\pi l^2)^{1/4}} \exp\left(-\frac{z^2}{2l^2}\right), \tag{8}$$

with $l = \sqrt{\hbar/(m\omega_z)}$ being the characteristic length scale of the harmonic oscillator. Integrating out $\Psi_z(z)$, at the level of the Hamiltonian, leads to a rescaling of the interaction

$$g_{2D} = g \int dz |\Psi(z)|^4 = \frac{g}{\pi l^2} \int dz \exp\left(-\frac{2z^2}{l^2}\right) = \frac{g}{\sqrt{2\pi} l} = a_s \sqrt{\frac{8\pi\hbar^3\omega_z}{m}}. \tag{9}$$

In the following, $n$ will correspond to the 2D atom density $|\Psi(x, y)|^2$, $g$ will denote the two-dimensional coupling $g_{2D}$, and $\Psi_{2D}$ will be refereed to as $\Psi$.

## 2.4. Bogoliubov Approximation

To describe the dynamics of small density excitations on top of the mean field, the population of higher momenta $N_{p\neq 0}$ can again taken into account. This is done by the

ansatz $\Psi \rightarrow \Psi + \delta\Psi$, where $\delta\Psi$ is a complex-valued perturbation on top of the mean field. Plugging this ansatz into the GPE and keeping $\delta\Psi$ to leading order yields

$$i\hbar\frac{\partial\delta\Psi}{\partial t} = \left[-\frac{\hbar^2}{2m}\vec{\nabla}^2 + V(\vec{x}) + 2g|\Psi_0|^2\right]\delta\Psi + g\Psi_0^2\,\delta\Psi^*, \tag{10}$$

where the solution for the mean field $\Psi$ is subtracted. To solve this equation, the so-called Bogoliubov transformation is used [16]

$$\delta\Psi = e^{-i\mu_0 t/\hbar}\cdot\sum_{\vec{p}\neq 0}\left(u_{\vec{p}}\,(\vec{x})e^{-i\omega_{\vec{p}}\,t} - v^*_{\vec{p}}\,(\vec{x})e^{i\omega_{\vec{p}}\,t}\right), \tag{11}$$

where $u_{\vec{p}}$ and $v_{\vec{p}}$ are the normal modes of the system and $\hbar\omega_{\vec{p}}$ their corresponding eigenenergies. Plugging this ansatz into Equation (11) and collecting the terms with $e^{i\omega_{\vec{p}}\,t}$ and $e^{-i\omega_{\vec{p}}\,t}$ yields the Bogoliubov-de Gennes equation:

$$\left[-\frac{\hbar^2}{2m}\nabla^2 - \mu_0 + V(\vec{x}) + 2gn\right]u_{\vec{p}}\,(\vec{x}) - gnv_{\vec{p}}\,(\vec{x}) = \hbar\omega_{\vec{p}}\,u_{\vec{p}}\,(\vec{x}), \tag{12}$$

$$\left[-\frac{\hbar^2}{2m}\nabla^2 - \mu_0 + V(\vec{x}) + 2gn\right]v_{\vec{p}}\,(\vec{x}) - gnu_{\vec{p}}\,(\vec{x}) = -\hbar\omega_{\vec{p}}\,v_{\vec{p}}\,(\vec{x}), \tag{13}$$

Without an external potential, i.e $V(\vec{x}) = 0$ and $\mu_0 = gn$, this can be diagonalized analytically by the ansatz $u_{\vec{p}}\,(\vec{x}) = u_{\vec{k}}\exp(i\vec{k}\vec{x})$ and $v_{\vec{p}}\,(\vec{x}) = v_{\vec{k}}\exp(i\vec{k}\vec{x})$, with $\vec{k} = \vec{p}/\hbar$, yielding the eigenenergies

$$\hbar\omega = \sqrt{\frac{\hbar^2k^2}{2m}\left(\frac{\hbar^2k^2}{2m} + 2ng\right)}, \tag{14}$$

know as the Bogoliubov dispersion relation, where $k$ is the absolute value of $\vec{k}$. Negative energy solution have been omitted. For small $k$, i.e., in the phonon regime where the wavelength is much larger than the healing length, or equivalently $\hbar\omega \gg \mu_0$, the dispersion becomes linear

$$\hbar\omega = \hbar k\sqrt{\frac{ng}{m}}, \tag{15}$$

allowing us to define a speed of sound

$$c_s = \sqrt{\frac{ng}{m}}. \tag{16}$$

For large $k$, i.e., in the free-particle regime, the dispersion relation becomes quadratic

$$\hbar\omega = \frac{\hbar^2k^2}{2m} + ng. \tag{17}$$

In an inhomogeneous external potential, the speed of sound is described in the local density approximation, which assumes a locally homogeneous density. This allow us to replace $n$ with $n(\vec{x})$, this is only valid for sufficiently smooth densities. By also being able to control the global interaction strength $g$ in time, through adjusting the scattering length $a_s$ using an external homogeneous magnetic field (via a so-called Feshbach resonances) [17, 18], the speed of sound can be controlled in time and space

$$c_s(\vec{x}, t) = \sqrt{\frac{n(\vec{x})g(t)}{m}}. \tag{18}$$

## 2.5. Numerical Simulation Methods

Analytic solutions for the GPE, especially for time dynamics, can only be found for specific cases, therefore numerical simulations need to be used. The following section describes the numerical method for imaginary time propagation to find the ground state of the quasi 1D-GPE, as well as the real-time propagation method to calculate time evolution. The simulations allows to compare the relevant parameter regimes with the 2D experiments. This section is based on Appendix B in the PhD thesis of Eike Nicklas [19], who also wrote the real and imaginary time propagation code.
The derivation for the quasi 1D-GPE is analogous to the quasi 2D-GPE derivation in Section 2.3. Here, a confining harmonic potential with a trapping frequency $\omega_\perp$ in the $y$- and $z$-directions is used. The wavefunction is again factorized $\Psi = \Psi_{1\mathrm{D}}(x,t) \cdot \Psi_\perp(y,z)$, but if the trapping is too shallow, the nonpolynomial nonlinear Schrödinger Equation (NPSE) provides a more accurate description. This formulation allows the Gaussian ground state to have a variable width along the $x$-direction, given by $\sigma^2(x) = l_\perp^2\sqrt{1+2a_s|\Psi_{1\mathrm{D}}(x)|^2}$, where $l_\perp = \sqrt{\hbar/m\omega_\perp}$ is the characteristic harmonic oscillator length. Integrating out the transverse coordinates within this ansatz leads to the NPSE [20]:

$$i\hbar\frac{\partial\psi_{1\mathrm{D}}}{\partial t} = \left[-\frac{\hbar^2}{2m}\frac{\partial^2}{\partial x^2} + V + \frac{g|\psi_{1\mathrm{D}}|^2}{2\pi l_\perp^2}\frac{1}{\sigma^2/l_\perp^2} + \frac{\hbar\omega_\perp}{2}\left(\frac{1}{\sigma^2/l_\perp^2} + \sigma^2/l_\perp^2\right)\right]\psi_{1\mathrm{D}}. \tag{19}$$

When $a_s|\Psi_{1\mathrm{D}}(x)|^2$ is much smaller than 1, the width $\sigma$ reduces to $l_\perp$, and the NPSE reduces to the 1D-GPE with a rescaled interaction $g_{1\mathrm{D}} = g/(2\pi l_\perp^2)$.
For numerical simulations, the wavefunction is discretized on a spatial grid with $N_g$ grid points. Therefore, the wavefunction can be represented by a vector of size $N_g$, and the Hamiltonian by a $N_g \times N_g$ matrix. The distance $\Delta x$ between two grid points must be chosen to be smaller than the smallest expected feature, so at least much less than the healing length. To find the ground state, imaginary time propagation (ITP) is used. In quantum mechanics, the time evolution of the wavefunction is given by the unitary time evolution operator $\hat{U}(t_0,t) = \exp\left(-i\int_{t_0}^{t}\hat{H}dt'/\hbar\right)$. Considering only a small time step $\Delta t$, the evolution in the wavefunction is given by

$$\Psi(x, t_0 + \Delta t) = e^{-i\hat{H}\Delta t/\hbar}\,\Psi(x, t_0). \tag{20}$$

Replacing $\Delta t$ with $-i\Delta t$ in Equation (20) and rewriting $\Psi(x, t_0)$ as a superposition of energy eigenstates $\Phi_\nu(x)$, i.e. $\Psi(x, t_0) = \sum_\nu a_\nu(t_0)\Phi_\nu(x)$, and yields

$$\Psi(x, t_0 - i\Delta t) = \sum_\nu e^{-E_\nu \Delta t/\hbar} a_\nu(t_0)\Phi_\nu(x), \tag{21}$$

where $E_\nu$ is the eigenenergy and $a_\nu(t_0)$ the a complex amplitude. In this setting, the amplitudes decay with a decay rate directly proportional to the corresponding eigenenergy. As a result, the lowest energy eigenstate decays the slowest [21]. By iterating over multiple imaginary time steps, the systems ground state obtained. After each step, the wavefunction is renormalized to conserve particle number, as the operation is not unitary. The simulation terminates when the relative energy between two steps falls below a specified threshold.
For each time step the matrix exponential $e^{-\hat{H}\Delta t/\hbar}$ needs to be calculated. For this the so-called split-step Fourier transformation is used. One first splits the Hamiltonian into an interaction Hamiltonian that depends only on position and a kinetic Hamiltonian, which depends only on momentum: $e^{-i\hat{H}} = e^{-i(\hat{H}_p + \hat{H}_x)\Delta t/\hbar}$. The interaction Hamiltonian $\hat{H}_x$ is diagonal in real space, making its matrix exponential easy to compute. In contrast, the kinetic Hamiltonian, $\hat{H}_p$, is diagonal in momentum space, making it more convenient to compute it in momentum space. Therefore it would be ideal to apply the kinetic Hamiltonian in Momentum space and the interaction Hamiltonian as well as the external potential in real space. This is achieved by splitting a single propagation step into three steps using the first order of the Baker-Campbell-Hausdorff formula, as proposed in [22]:

$$\psi(x, t - i\Delta t) = e^{-(\hat{H}_p + \hat{H}_x)\Delta t/\hbar}\, \psi(x, t) \approx e^{-\hat{H}_p \Delta t/2\hbar}\, e^{-\hat{H}_x \Delta t/\hbar}\, e^{-\hat{H}_p \Delta t/2\hbar}\, \psi(x, t). \tag{22}$$

Because $\hat{H}_p$ and $\hat{H}_x$ generally do not commute, this is only approximate to the order $\mathcal{O}[(\Delta t)^3]$. Therefore, $\Delta t$ has to be chosen small enough to avoid numerical errors [22, 23]. A full time step starts by performing a fast Fourier transform (FFT) of the wavefunction $\Psi(x, t)$ and applying half a time step by multiplying $\mathscr{F}(\Psi(x, t))$ with the matrix $e^{-i\hat{H}_p \Delta t/2\hbar}$. Then, the wavefunction is transformed back to real space to perform a time step by multiplying $\Psi(x, t)$ with the matrix $e^{-i\hat{H}_x \Delta t/2\hbar}$. Lastly, the wavefunction is transformed to momentum space again, and half a time step is applied as before. Performing multiple FFTs per time step is still much faster than calculating a matrix exponential of a non-diagonal matrix.
Performing the real time evolution is done straightforward: by replacing $-i\Delta t$ with $\Delta t$, the previously described split-step fast Fourier transformation method can be used. This further restricts $\Delta t$, as it needs to be much smaller than all expected characteristic timescales, especially $\Delta t \ll \hbar/\mu_0$, where $\mu_0$ is the chemical potential.

## 2.6. Dipole Potential

To create a conservative light potential for the atom the so-called dipole force is used. The light-atom interaction, when the light is far off resonance to any atomic transition, can be described purely in classical terms. Instead of exciting the atom, the electric field from the light induces an electric dipole moment $\vec{\mu}$ in the atom. This results in an energy change $E = -\vec{\mu} \cdot \vec{E}$. The energy change is either positive or negative depending on the relative orientation between $\vec{\mu}$ and $\vec{E}$. In this picture, the atom behaves like a driven harmonic oscillator with the resonance frequency $\omega_0$, driven by an electric field with the frequency $\omega_l$. When $\omega_l \ll \omega_0$ (red detuned), the induced dipole follows the electric field, aligning $\vec{\mu}$ and $\vec{E}$ in parallel, leading to a decrease in energy (i.e., attractive). For $\omega_l \gg \omega_0$ (blue detuned), the induced dipole is exactly $\pi$ out of phase, making $\vec{\mu}$ and $\vec{E}$ anti-parallel, resulting in an increasing energy (i.e., repulsive). In the case of a spatially dependent light field, this results in a dipole potential, directly proportional to the light intensity $I(\vec{x})$,

$$U(\vec{x}) = -\frac{3\pi c^2 \Gamma}{2\omega_0^2 \Delta} I(\vec{x}), \tag{23}$$

where $c$ is the speed of light, $\Gamma$ is the harmonic oscillator damping, and $\Delta = \omega_0 - \omega_l$ is the detuning. A rigorous derivation of Equation (23) using perturbation theory can be found in [24]. The damping of the harmonic oscillator can be assigned to the natural linewidth of the transition. For a real atom, multiple transitions must be considered. For the alkali atom $^{39}$K, these are the $2S_{1/2}$ to $2P_{1/2}$ transition, also known as the D1-line, and the $2S_{1/2}$ to $2P_{3/2}$ transition, also known as the D2-line. For linearly polarized light, the dipole potential is given by

$$U(\vec{x}) = -\frac{\pi c^2 \Gamma}{2\hbar\omega_0^3} \left( \frac{1}{\Delta_1} + \frac{2}{\Delta_2} \right), \tag{24}$$

where $\Delta_{1/2}$ are the detuning to the D1/D2-lines, respectively [24].

## 2.7. Experimental Setup: Cooling, Trapping and Imaging

All of the following experimental data has been produced using a quasi-two-dimensional Bose-Einstein Condensate of $^{39}$K: the BECK experiment. This section provides a short overview of the experimental apparatus, especially the cooling, trapping, and the imaging processes. A more detailed description can be found in [25, 26].
The atoms need to be cooled well below room temperature to achieve condensation; since collisions with room-temperature atoms heat up the sample, all subsequently mentioned processes take place inside an ultra-high vacuum system. An oven heated to approximately 70 °C provides a background vapor of thermal potassium atoms. Using four orthogonal counter-propagating beams, the atoms are trapped in a two-dimensional magneto-optical trap (MOT). The atoms are transferred through a differential pumping

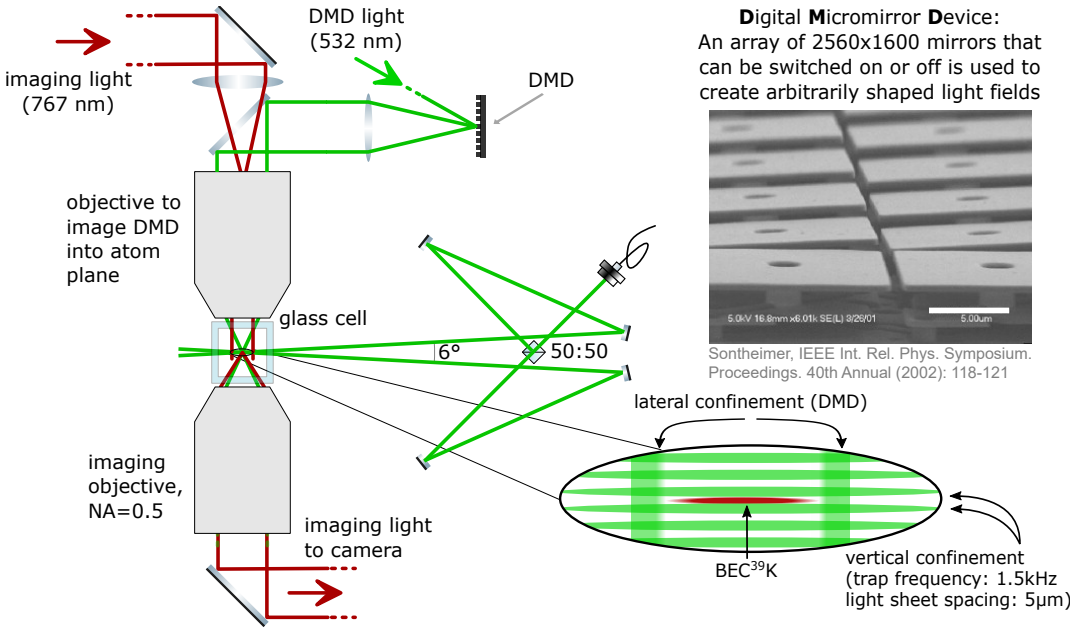



Figure 2.2: **Overview of the Experimental Setup.** At the end of the cooling process, the atoms are loaded into a vertically confining optical dipole trap created by two interfering repulsive laser beams, leading to a trap frequency of 1.5 kHz. This creates a quasi-two-dimensional BEC. Confinement in the $xy$ plane is achieved by shaping a collimated beam with a digital micromirror device DMD and projecting it through an objective onto the atoms. Imaging is performed via absorption imaging. The figure is adapted from the BECK group.

stage and are then loaded into a 3D-MOT. The 3D-MOT is located in a low-pressure region, and a glass cell provides good optical access. To further increase the atom density, a compressed MOT is used. Sub-Doppler cooling is achieved via gray molasses. Next, a magnetic trap confines the atoms of the $|F, m_f\rangle = |1, -1\rangle$ state and adiabatically compresses the cloud. At zero magnetic field $^{39}$K has a negative scattering length of $a_{bg} = (-29.3 \pm 0.3)a_0$ [27], which makes condensation of large clouds impossible. Therefore, the atoms are loaded into an attractive optical dipole trap (1064 nm), and the scattering length is adjusted to a positive value by applying a homogeneous magnetic field near the Feshbach resonance at $(561.12 \pm 0.02)$ G [27]. Condensation is reached by evaporative cooling, which means slowly lowering the dipole trap depth. A magnetic field gradient is used to levitate the cloud, counteracting gravitational forces.
The condensed atoms are then loaded into the final repulsive dipole trap, where the $z$-confinement is realized by two interfering laser beams (532 nm). The minima of the interference pattern are spaced by 5 µm, resulting in a harmonic trap in the $z$ direction with a trap frequency $\omega_z = 2\pi \times 1.5$ kHz and achieving quasi-two-dimensionality. The atoms ($\sim 50000$) now have a temperature of roughly 20 nK.

The atom cloud can now be well described by the quasi-two-dimensional GPE, where the interaction strength $g$ and external potential $V(\vec{x})$ can be precisely controlled, as explained in the following. The interaction strength can be globally controlled by adjusting the scattering length with a homogeneous magnetic field $B$, through the use of a Feshbach resonance. The magnetic field is produced by two coils in a Helmholtz configuration. The functional dependence of $a_s$ on $B$ is given by

$$a_s = a_{bg}\left(1 - \frac{\Delta}{B - B_0}\right), \tag{25}$$

where $a_{bg} = (-29.3 \pm 0.3)a_0$ is the background scattering length, $B_0 = (561.12 \pm 0.02)\,\mathrm{G}$ is the resonance position, and $\Delta = (56.7 \pm 0.9)\,\mathrm{G}$ is the width of the resonance [27]. The external potential $V(\vec{x})$ is created by illuminating a digital micromirror device (DMD) with a collimated Gaussian beam at a wavelength of 532 nm. The DMD consists of $2560 \times 1600$ micromirrors, each of which can be individually set to **on** or **off** configuration. In the **on** state, the light is projected and demagnified by a factor of 1/86.7 through an objective, with an numerical aperture (NA) of 0.5, onto the atoms. Due to the limited spatial resolution of the objective and the high demagnification, a single micromirror can not be resolved in the atom plane. The diffraction limit is $d = \lambda/(2 \cdot \mathrm{NA}) = 0.5\,\mu\mathrm{m}$ and the size of a single micromirror is $7.6 \times 7.6\ \mu\mathrm{m}^2$, resulting in $6 \times 6$ mirrors being unresolved. This allows projecting arbitrary light potentials with 36 grayscale level onto the atom cloud. An iterative feedback optimization algorithm is used, to improve the light potential created by the DMD [28]. In short, the algorithm adjusts the DMD pattern based on the measured density distribution, comparing it to the desired ideal distribution. This allows the correction of small imperfections in the light potential. The atom cloud is imaged by illuminating the atoms with resonant light at 767 nm and measuring the absorption signal with a CCD camera. Absorptive imaging heats and destroys the condensate and therefore the entire experimental cycle is repeated for each for each shot. A single experimental cycle takes about 15 seconds

# 3. Wavepacket Analysis

The goal of this Section is to understand why, a potential of the form

$$V(r) = \begin{cases} 0 & r < R, \\ \beta \cdot (r - R) & r \geq R, \end{cases} \tag{26}$$

which we call a slanted box (slox) potential, suppresses the coherent reflection of phonons, while still conserving the atom number. With this absorptive behavior, the slox potential effectively mimics an infinitely extended system, which is useful since most theoretical frameworks assume such a system. The potential was experimentally observed to of importance when performing measurements on spontaneous pattern formation [10]. While patterns emerged in a harmonic trapping configuration, they could not be systematically reproduced in a box trap, which is essentially a slox with a slope $\beta \to \infty$. The slox trap combines key elements of these two configurations—a homogeneous density in the center and a tapered density at the edges. A detailed analysis of pattern formation in the slox potential can be found in Section 4.

To test the reflectivity of the slox potential, a wavepacket is prepared in the middle of the condensate, which then propagates radially outward. In Section 3.1, the preparation of the wavepacket in the experiment will be explained. It will be shown that only for a steep slox potential (high $\beta$) the wavepacket reflects at the boundary. Section 3.2 is dedicated to understanding the underlying mechanisms for the absorptive nature of the slox potential by performing 1D-GPE simulations and examining the influence of various wavepacket and potential parameters, as well as other aspects of the simulation. In Section 3.3, it is shown that static noise on the light potential leads to the destruction of the wavefront and is the main reason why the slox potential does not allow coherent reflection. In Section 3.4, artificial noise will be added to the light potential to test which structural noise is best suited for implementing absorptive boundaries. In Section 3.5, an entirely different method for implementing absorptive boundaries in both experiment and simulation is presented, using the concept of hyperbolic space. Additionally, in Appendix A discusses challenges encountered while implementing this new hyperbolic boundary in the experiment. To solve these, a new calibration for the iterative optimization algorithm is presented.

## 3.1. Experimental Wavepacket Preparation and Propagation in Slox Potential with Different Slopes

A wavepacket is prepared by allowing the system to equilibrate in a trapping potential with a small round bump in the middle. As expected from the Thomas-Fermi approximation (Section 2.2), this leads to a condensate with a dip in the center. The bump

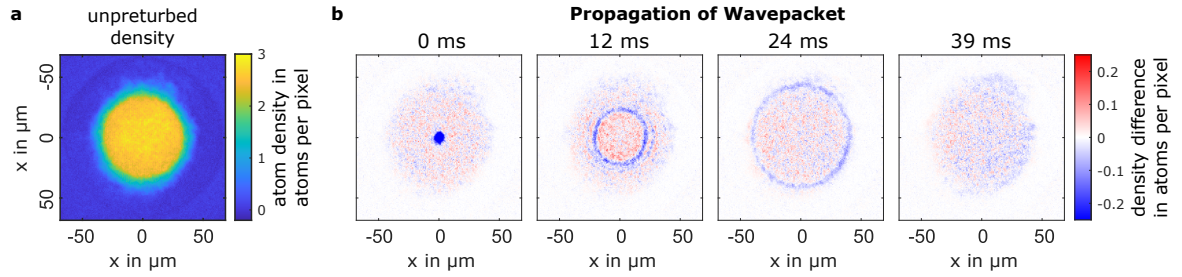



Figure 3.1: **Experimental Wavepacket Preparation and Propagation.** **a**, The unperturbed density for a slox potential with a slope of $\beta \sim 28\,\mathrm{Hz\,\mu m^{-1}}$ and a radius of $R = 30\,\mu\mathrm{m}$. The density is flat in the middle and linearly decreases at the edges. **b**, A wavepacket is prepared by equilibrating the system with a bump in the middle of the potential, which is then suddenly flattened, causing the wavepacket to propagate radially outward. For a slox potential with a slope of $\beta \sim 28\,\mathrm{Hz\,\mu m^{-1}}$, no coherent reflection of the wavepacket at the boundary is observed (leftmost image).

in the potential is then suddenly removed at time $t = 0$ by turning off the corresponding mirrors on the DMD. This out-of-equilibrium system evolves in time, leading to a wavepacket radial propagation outward. This wavepacket can be described as a superposition of Bogoliubov phonons, traveling at the speed of sound ( Section 2.4). For a measurement series, the system is always prepared in the same way, and destructive imaging is performed at different times $t$ relative to $t = 0$ to study the wavepacket dynamics.

Figure 3.1a shows the unperturbed atom density with a chemical potential $\mu_0$ of roughly 280 Hz in a slox with a slope of $\beta \sim 28\,\mathrm{Hz\,\mu m^{-1}}$ and a radius of $R = 30\,\mu\mathrm{m}$. The density is approximately flat in the center and starts to decrease linearly at $r = R = 30\,\mu\mathrm{m}$. The wavepacket propagation is shown in Figure 3.1b. Here, the rescaled density difference $\delta n(\vec{x}, t) = \sqrt{n_0(\vec{x})/\bar{n}_0^3}\,(n(\vec{x}, t) - n_0(\vec{x}))$ is used to better visualize the wavepacket. The background density without the dip is denoted by $n_0$ and $\bar{n}_0$ is the the mean density in the center of the condensate. The normalization is chose such the density difference is proportional to the phononic excitation [8, 29]. The images for each time are an average of approximately 30 single shots. The wavepacket propagates radially outward, while decreasing in amplitude proportional to $1/r$. The wavepacket slows down at the boundary, which can be explained by the local density approximation: $c_s(\vec{x}) \sim \sqrt{n(\vec{x})}$. After interacting with the boundary, no clear reflection of the wavepacket is observed.

To analyze the behavior of the wavepacket, especially the reflectivity of the slox potential for various slopes, this wavepacket propagation was performed for slox potentials with slopes of $\beta = 14,\ 28, 47\,\mathrm{Hz\,\mu m^{-1}}$ (shallow, normal, steep slox). Figure 3.2a shows the atom densities for these three slox potentials. As expected the slope of the density at the boundary becomes shallower as $\beta$ decreases. The average density in the center of

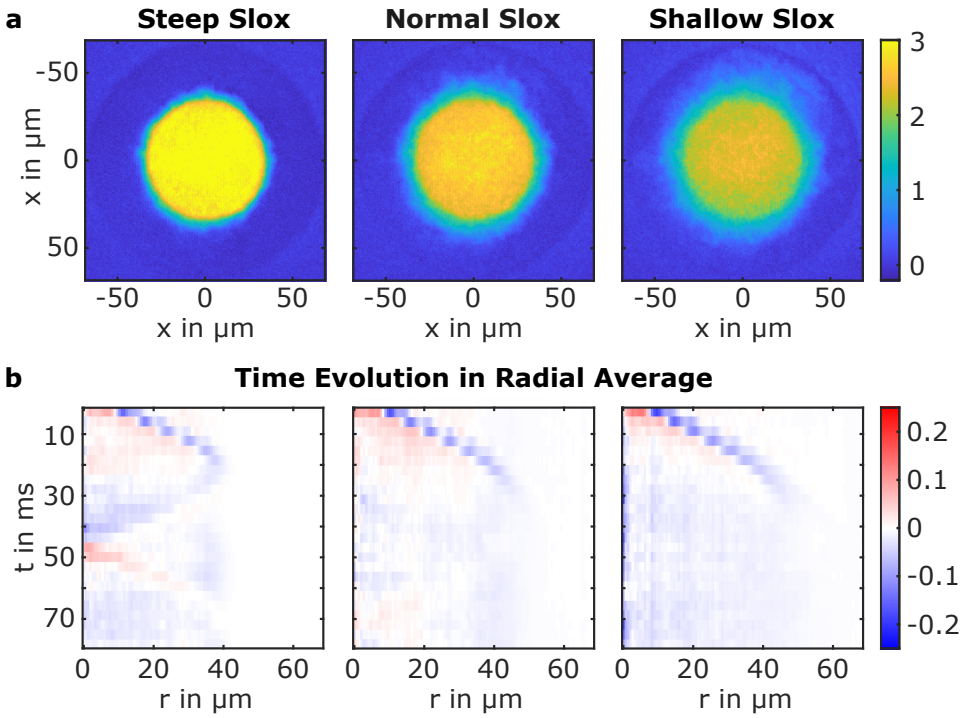



Figure 3.2: **Experimental Wavepacket Propagation in Slox Potentials with Different Slope. a**, Unperturbed density distribution for the slox potentials with slopes of $\beta = 14,\ 28, 47\,\mathrm{Hz\,\mu m^{-1}}$ (shallow, normal, steep slox). **b**, Wavepacket propagation in the corresponding potentials, visualized by the radially averaged density difference. Only for the steep slox is a coherent reflection observed.

the condensate slightly decreases, with decreasing $\beta$, because more atoms are located at the edge of the condensate. This also slightly decreases the speed of sound in this region.

To better visualize the propagation of the wavepacket, radial averages of the density differences $\delta n(\vec{x}, t)$ are calculated and shown in Figure 3.2b for the three different slox potentials. In this representation, the position of the wavepacket over time can be nicely tracked. Especially in the case of the normal and shallow slox, the decrease in wavepacket speed near the boundary can be observed. A reflection of the wavepacket is observed only for the steep slox. The atom number for all three cases decreased by less the 0.8% over the whole measurement time, showing that the slox potential confines the atoms.

This observation coincides with the observation for the spontaneous pattern formation mentioned in the introduction and will be discussed in detail in Section 4. However, the mechanism behind the reflections is not understood, and will be studied numerically in the following Section.

## 3.2. Wavepacket Preparation and Propagation in 1D-GPE Simulation

Here, 1D-GPE simulations are performed to reproduce and understand the effect of the absorptive slox potential observed in the experiment. As will be seen Section 3.2.1, reproducing this effect is not straightforward. In the following Section, various parameters and aspects of the simulation will be tested to determine their influence on the reflectivity of the wavepacket. The 1D simulations are performed using imaginary- and real-time evolution, as explained in Section 2.5. 1D simulations are chosen instead of 2D simulations as they are far less computationally expensive, can be performed on a CPU, and can still mimic most physical features. Unless explicitly stated otherwise, the parameters in the following simulations are chosen similarly to the experimental conditions. The speed of sound is $c_s \sim 1.7\,\mu\mathrm{m\,ms^{-1}}$, the orthogonal trap frequency is $\omega_\perp = 2\pi \cdot 460\,\mathrm{Hz}$, the scattering length is $a_s = 125\,\mathrm{a_B}$, and with that, the chemical potential is $\mu \sim 280\,\mathrm{Hz}$, and the healing length is $\xi \sim 1\,\mu\mathrm{m}$. The radius of the slox potential $R = 35\,\mu\mathrm{m}$, and the slope $\beta \sim 28\,\mathrm{Hz\,\mu m^{-1}}$ are also chosen similarly to the experiment. The 1D density $n_{1\mathrm{D}}$ in the simulation and the 2D density $n_{2\mathrm{D}}$ in the experiment have different units and therefore cannot be directly compared. Thus, the density and density differences in the simulation are normalized to arbitrary units.

The grid spacing $\Delta x$ of $200\,\mu\mathrm{m}/2^{10} \approx 0.2\,\mu\mathrm{m}$ is much smaller than the healing length, and the simulation range is $200\,\mu\mathrm{m}$. The simulation boundaries at $\pm 100\,\mu\mathrm{m}$ are implemented as infinitely high potentials. Since the density is always effectively zero for $|x| \gtrsim 70\,\mu\mathrm{m}$, the simulation boundary should not affect the results. The time step $\Delta t$ is $5 \times 10^{-7}\,\mathrm{s}$ and therefore much smaller than $\hbar/\mu$. The time step $\Delta t$ can be increased by a factor of 3, and grid spacing $\Delta x$ by a factor of 4 before numerical errors accumulate or any significant changes in dynamics occur, confirming that these parameters are sufficiently small.

Preparing the wavepacket in the simulation is analogous to the experiment and is illustrated in Figure 3.3. First, the ground state for a given potential is calculated using imaginary time propagation. Then, a Gaussian wavepacket is added to the density, to explicitly mimic the dip imprinted in the experiment. This out-of-equilibrium wavefunction is then propagated in time using real-time propagation. The width of the wavepacket is chosen to be comparable to the experiment ($\sim 4\,\mu\mathrm{m}$), which is larger than the healing length and therefore mostly consists of phonon in the linear Bogoliubov dispersion relation regime. The density at different times (10, 20, 35 ms) is shown in Figure 3.3.

The dynamic of the wavepacket looks, at first glance, very similar to the experiment. The wavepacket propagates outward to the left and right and slows down when reaching the boundary. One difference to the experiment is that the amplitude of the wavepacket does not decrease as $1/|\mathrm{x}|$ in the simulation, as this is a feature of the two-dimensional

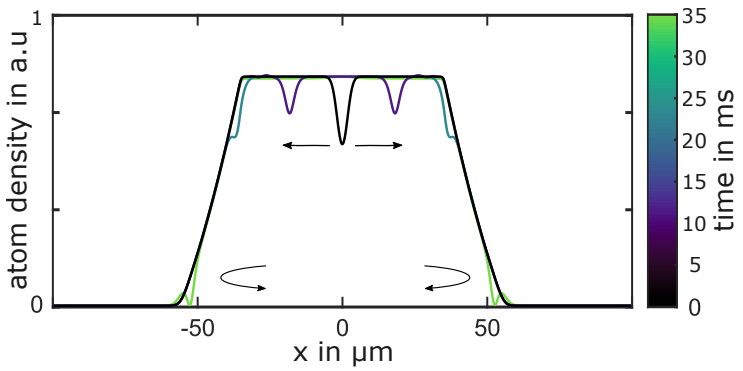



Figure 3.3: **Wavepacket Preparation and Propagation in 1D-GPE Simulation.** The wavepacket is prepared similar to the experiment: The ground state of the GPE with an external slox potential is calculated. Then, a Gaussian wavepacket is added to the wavefunction, and this out-of-equilibrium system is propagated in time. The density $n = |\Psi(x,t)|^2$ is shown for multiple times, indicated by the colorbar. As soon as the amplitude of the wavepacket equals the background density, the wavepacket is reflected.

nature of the experiment. Another key difference is that the wavepacket is reflected, as soon as the amplitude of the wavepacket becomes equal to the background density. This effect has also been observed for so-called gray and dark solitons in experiments, simulations and has been theoretically explained [30, 31, 32] and will be discussed in detail in Section 3.2.3. Therefore, despite the similar parameters to the experiment, the simulation show high levels of the reflection in the slox potential. In the following, we study whether this reflection also occurs for shallower slox potentials.

### 3.2.1. Wavepacket Propagation in Slox Potential with Various Slopes

Reproducing the effect of the absorptive slox potential in simulations is important to understand the mechanism behind it. As a first test, simulations with variable slopes of the slox potential $\beta$ were performed. To visualize the dynamics of the wavepacket, the atom density $n(x,t) = |\Psi(x,t)|^2$ is plotted in a $t$-$x$ diagram, where the density is represented by color. This allows a direct comparison with the radial average over time from the experiment. Figure 3.4 shows the wavepacket propagation in slox potentials with various slopes (decreasing from left to right).
In contrast to the experiment, a clear reflection of the wavepacket is observed for all slopes. Furthermore, the wavepacket does not change in width or amplitude after being reflected. This indicates that there must be some parameter difference or an effect not captured by the simulation method. To determine the key differences, various wavepacket parameters, trapping conditions, and simulation methods are quantitatively examined in the following Sections.

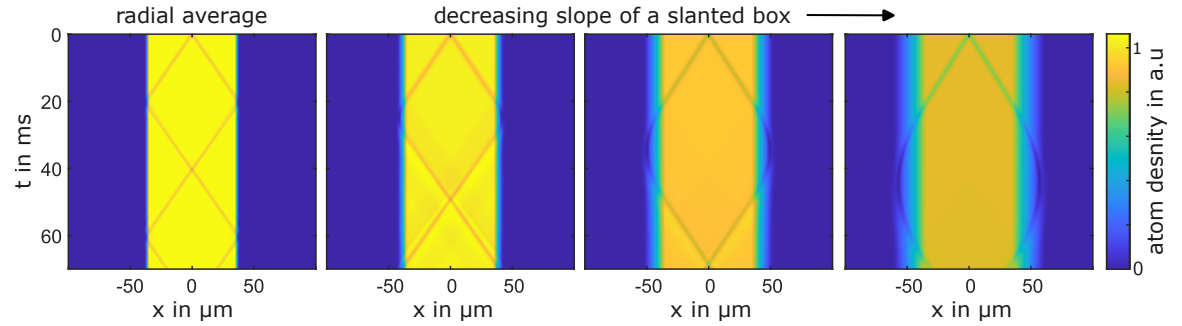



Figure 3.4: **Wavepacket Propagation in Slox Potential with Various Slopes.** Simulated wavepacket dynamics for slox potentials with decreasing slopes $\beta$ (left to right). The $t$-$x$ diagrams show atom density $n(x,t) = |\Psi(x,t)|^2$, where the amplitude is represented by color. Surprisingly, in constrast to the experiment, clear wavepacket reflections are observed for all slopes without changes in width or amplitude after reflection.

### 3.2.2. Propagation of Wavepackets with Various Widths

One parameter of the wavepacket that could influence the reflection is its width. Therefore, simulations with varying widths have been performed. These simulations were performed in a slox potential with a slope of $\beta \sim 28\,\mathrm{Hz\,\mu m^{-1}}$. Figure 3.5 shows the propagation of the wavepacket in the density difference, defined as $\delta n(x,t) = n(x,t) - n_0$, where the background density $n_0$ without the wavepacket is subtracted to better visualize the wavepacket propagation.

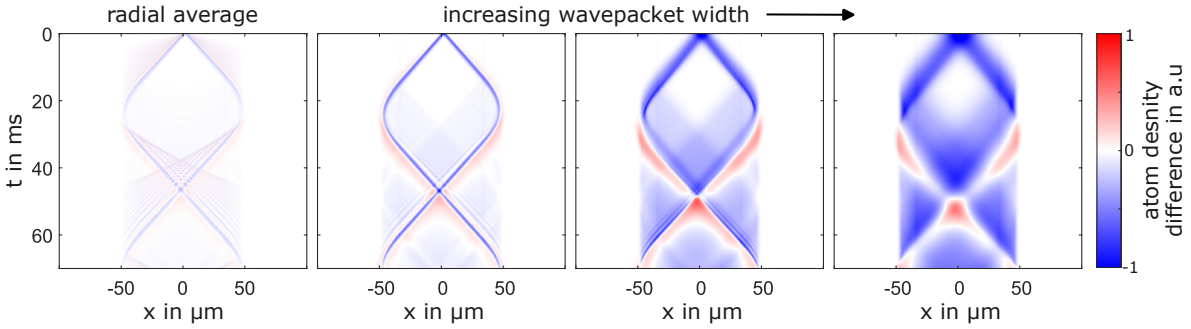



Figure 3.5: **Propagation of Wavepackets with Various Widths.** Simulation results for wavepackets of varying widths in a slox potential with a slope of $\beta \sim 28\,\mathrm{Hz\,\mu m^{-1}}$. For narrow wavepackets, high-$k$ components beyond the linear Bogoliubov regime cause fast-moving density ripples, which are reflected at the boundary. For broader wavepackets, reflection occurs without significant spreading or changes in width, demonstrating that wavepacket width has minimal impact on reflectivity.

Because a wavepacket can be described as a superposition of waves with specific wavenumbers $k$, a narrower wavepacket in real space corresponds to a broader wavepacket in momentum space. Therefore, the narrowest wavepacket (leftmost images) includes contributions from momentum components that extend beyond the linear regime of the Bogoliubov dispersion relation discussed in Section 2.4. The effects of this are visible in the density ripples that move significantly faster than the speed of sound. These high-$k$ waves are also reflected at the boundary, as seen at later times when they reappear inside the condensate. In the experiment, ravepackets are always prepared in such a way that the high momentum components are negligible.

For the other three widths, the wavepacket does not include higher-momentum components, and reflection occurs even as the wavepacket width approaches the size of the entire boundary. This demonstrates that the width of the wave packet does not significantly impact reflectivity, as in all cases, when the density approaches zero, the nonlinear effects of the Bogoliubov dispersion relation are present.

### 3.2.3. Propagation of Wavepackets with Various Amplitudes

Simulations with various amplitudes of the wavepacket were performed, with the results are shown in Figure 3.6. Here, the trap parameters are $R = 35\,\mu\text{m}$ and $\beta \sim 28\,\text{Hz}\,\mu\text{m}^{-1}$. For the three smallest amplitudes, the reflections are similar to those already observed in previous simulations. It appears that even a very shallow wavepacket is reflected without any perturbation.

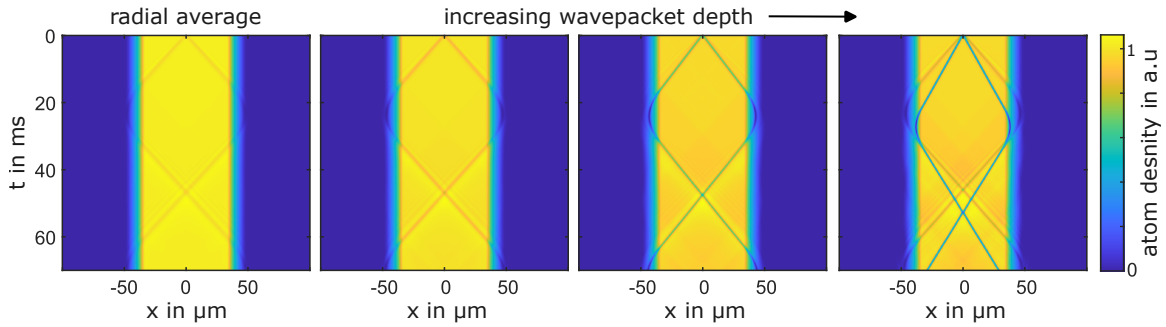



Figure 3.6: **Simulation Results for Wavepackets of Various Amplitudes.** For shallow wavepackets, reflections are similar to earlier observations, i.e. reflection occurs when the perturbation's amplitude equals the background condensate density. For deeper wavepackets, the dynamics are better described by the motion of a gray and dark solitons in a slowly varying external potential.

For a very deep wavepacket, where the wavepacket amplitude approaches the height of the background condensate, an interesting effect is observed (rightmost images). The velocity of such a perturbation is slower than the speed of sound, which cannot be explained by the Bogoliubov dispersion relation discussed in Section 2.4. This is reasonable because the key assumption for the Bogoliubov approximation is that the perturbation has a small amplitude. The observed effect corresponds to a topological defect known as gray and dark solitons. It is observed that the perturbation is reflected as soon as its amplitude matches the background condensate's density. The consistent reflection of both solitons and wavepackets with lower amplitudes, when the amplitude of the perturbation equals the background density, suggests that a wavepacket in a region of decreasing background density can be increasingly well described as gray and dark solitons, instead of Bogoliubov phonons. This could explain how the reflection of wavepacket at the boundary can be understood. This raises the question if 1D Simulation are appropriate for comparison with the 2D experiments, as in 2D solitons quickly decay into vortices [33].

Figure 3.7b shows the measured speed of the perturbation compared to the speed of sound expected from the local density approximation at the position of the perturbation, for a simulation shown in Figure 3.7a. In the flat region of the condensate, these two speeds match perfectly. However, shortly after the beginning of the boundary, the actual speed of the perturbation starts to deviate from the prediction of the local density approximation. The actual speed is smaller and decreases linearly to $0\,\mu\mathrm{m\,ms}^{-1}$, supporting the explanation that the wavepacket gradually transforms into a gray, and eventually, a dark soliton. This effect has already been observed for gray and dark soli-

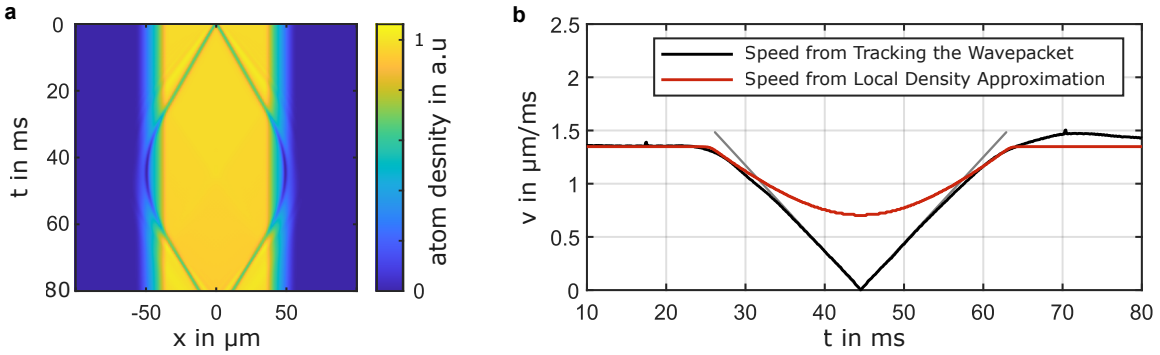



Figure 3.7: **Local Density Approximation vs. Extracted Speed. a**, Atom density during the propagation and reflection of a wavepacket. **b**, Comparison of the extracted speed of the perturbation with the speed predicted by the local density approximation at the position of the perturbation,. While the two match in flat region of the condensate, deviations occur at the boundary, indicating a transition from Bogoliubov phonons to soliton-like behavior. The theoretically predicted speed of a soliton decreases linearly at the boundary of a slox potential, indicated by the gray lines.

tons in simulations and experiments with different trap geometries [30, 31]. The motion of gray and dark solitons in a slowly varying external potential is theoretically described in [32]. The equation of motion for a soliton in a slox potential is given by

$$\ddot{x}(t) = -\frac{1}{2}V'(x) \sim \begin{cases} 0 & x < R, \\ -\beta & x \geq R, \end{cases} \tag{27}$$

which means that the speed is constant in the flat region of the condensate and decreases linearly until turning around at the boundary, as indicated by the gray lines in Figure 3.7b. This coincides with the behavior extracted for the wave packet. Seemingly the perturbation does not directly transform back into a wavepacket described by Bogoliubov phonons, as can be seen in the higher speed of sound in the flat part of the condensate after the reflection.

### 3.2.4. Wavepacket Simulation in 2D Assuming Radial Symmetric Solution

Another aspect that differs between the simulation compared to the experiment is the dimensionality. A full 2D-GPE was not simulated; instead, a 2D-GPE assuming a radially symmetric solution was used. To do so, we can write the kinetic term of the 2D-GPE in polar coordinates $\nabla^2 = \frac{\partial^2}{\partial r^2} + \frac{1}{r}\frac{\partial}{\partial r} + \frac{1}{r^2}\frac{\partial^2}{\partial \theta^2}$ and assume that the wavefunction has no dependence on the polar angle $\theta$. With this ansatz, the kinetic term looks similar to the kinetic term for a 1D-GPE but includes an extra $\frac{1}{r}\frac{\partial}{\partial r}$ term. To simulate such an equation a different simulation was used that works not by the split-step Fourier transformation but by the Backward Euler finite difference (BEFD) method, which is explained in [21]. The simulation code was provided by Nikolas Liebster. This method is significantly slower, and therefore only a single simulation run was conducted.

For this simulation, the wavepacket is again Gaussian, centered around $r = 0$, and added to the ground state wavefunction. The time evolution of the density and the density differences are shown in Figure 3.8a and b. The wavepacket amplitude decreases towards the edges with $1/r$, as observed in the experiment, and is reflected at the boundaries. The reflection occurs again when the amplitude of the perturbation equals the background density. For the chosen parameters, this happens later compared to the 1D simulation due to the decrease in the amplitude of the perturbation toward the edge. Figure 3.8b shows the extracted speed of sound of the perturbation (black) and the speed of sound predicted by the local density approximation (red) at the position of the wavepacket. The two speeds match in the flat region of the condensate but start to deviate towards the edges of the condensate. The linear decrease in speed indicates a transition from Bogoliubov phonons to soliton-like behavior. This behavior is very similar to what is observed in the 1D simulations. The expected decay of a soliton into vortices cannot be captured by a 2D simulation assuming radial symmetry. To further investigate the reflection in the case of a 2D condensate, a 2D simulation must be performed, which

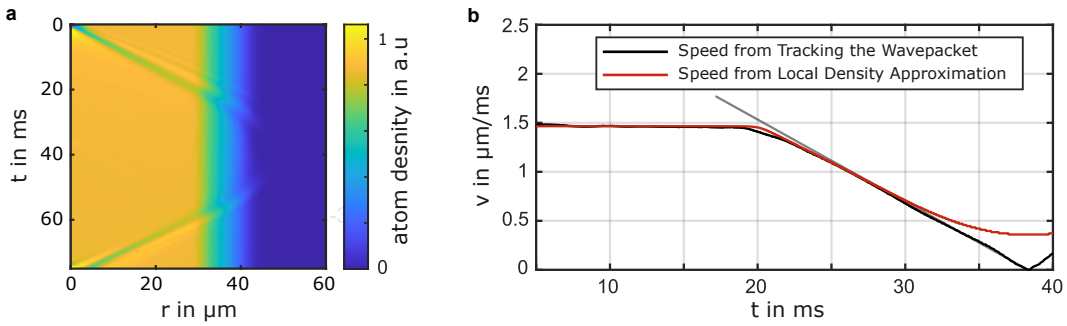



Figure 3.8: **Wavepacket Simulation in 2D Assuming Radial Symmetric Solution.** By assuming the wavefunction has the form $\Psi(r,t)$ and the dynamics are described by a 2D-GPE, allows it to be simulated like a 1D-GPE, with the kinetic term $\frac{\partial^2}{\partial x^2}$ replaced by $\frac{\partial^2}{\partial r^2} + \frac{1}{r}\frac{\partial}{\partial r}$. **a**, The time evolution of the atom density with a Gaussian wavepacket added around $r = 0$ at $t = 0$ inside a slox potential. **b**, Comparison of the extracted speed of the perturbation with the speed predicted by the local density approximation. The theoretically predicted speed of a soliton at the boundary of the slox potential is linear, indicated by the gray lines.

remains a task for future work. The perturbation could only be tracked reliably up to about 40 ms, due to the low densities and interference with higher momenta, that got reflected earlier. However, the reflection appears symmetric in the density plot over time.

This short Section testing one potentially important difference between the experiment and simulation regarding reflection, shows that assuming 2D radial symmetry of the wavefunction is not accurate to describe the experiment. In general, radial symmetry cannot be assumed in the experiment, and this plays a significant role in the reflection at the boundary, as will be shown in the following Section 3.3.

### 3.2.5. Truncated Wigner Approximation

A notable difference between the experiment and the simulation is thermal or quantum noise in the real system. In simulations, this noise can be described using the truncated Wigner approximation. The idea behind this approximation is to calculate the ground state as before and then add additional noise to the wavefunction. The total wavefunction is then propagated in time, and the observable (in this case, the density $n(x,t)$) is averaged over many noise realizations. The noise is chosen in a specific way to properly mimic quantum noise. It takes the form

$$\Psi_{\text{Noise}} = \sum a_i \psi_i(x), \tag{28}$$

where $\psi_i$ are the eigenfunctions of the system, and $a_i$ are randomly sampled complex numbers with a mean amplitude of $\langle |a_i| \rangle = 1/2$ [34]. For simplification, the eigenfunctions are approximated by the eigenfunctions of a box potential with a width equal to

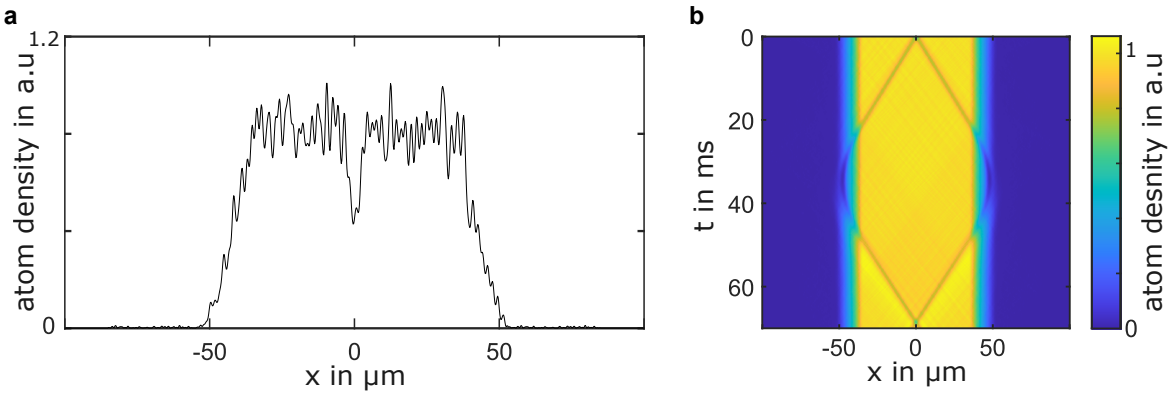



Figure 3.9: **Truncated Wigner Approximation.** **a**, Typical density distribution at $t = 0$, with noise added to the wavefunction. **b**, Dynamics in the atomic density over time, average over multiply realization. The wavepacket is reflected at the boundary.

the condensate size. As before, a Gaussian wavepacket is added on top of this wavefunction, and the time evolution of the atomic density $n(x, t)$ is averaged over 100 simulation runs. A typical initial density distribution at $t = 0$ is shown in Figure 3.9a. The average density distribution over time is displayed in Figure 3.9b. Even with the noise in the initial conditions, the reflection of the wavepacket is visible.

## 3.3. Accounting for Noise in the Light Potential

A visible difference between the experiment and the simulation is the static noise in the light potential. Figure 3.10a shows the averaged atom density for the shallow slox ($\beta = 47\,\mathrm{Hz\,\mu m^{-1}}$). Especially at the edge, the density distribution is not smooth and has grainy artifacts. This noise is stable from shot to shot and is visible in the averaged density. Therefore, a reasonable assumption is that the roughness in the atomic distribution arises from imperfections in the light potential. These small imperfections, caused by noise on the light beam projected on the DMD, can be adjusted for by using the feedback algorithm mentioned in Section 2.7.

The density distribution for the optimized light potential is shown in Figure 3.10d. It is significantly smoother, more uniform, and symmetric. For both the optimized and the non-optimized density distribution, a wavepacket is prepared with the DMD as described in Section 3.1. The time evolution is shown in the radial average density difference $\delta n(x, t)$ in Figure 3.10b and e. A direct comparison between the two shows a clear reflection in the optimized case and no coherent reflection in the non-optimized case.

Artificial noise was added to the potential in the 1D simulation to mimic this difference. The noise is generated as uncorrelated pixel noise, smoothed by Gaussian convolution with a width of $\sim 2\,\mu\mathrm{m}$. This is, of course, only a simplified noise model, aiming to

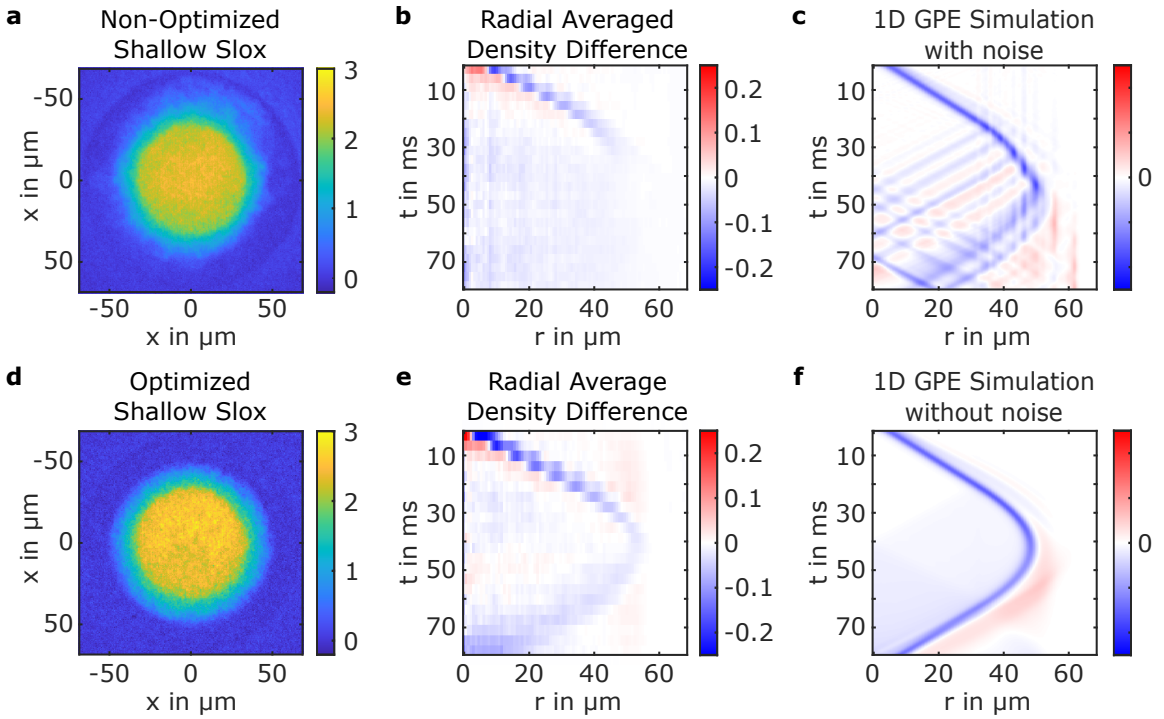



Figure 3.10: **Wavepacket Propagation in Rough and Smooth Slox Potential: Simulation and Experiment Comparison.** **a**, Average atomic density for the shallow slox potential ($\beta = 47\,\mathrm{Hz}\,\mu\mathrm{m}^{-1}$) without optimizing the light potential. **b**, Time evolution in the radial average density difference for the non-optimized slox potential. **c**, 1D-Simulation results with noise added to the potential. **d**, Average atomic density for the optimized light potential. **e**, Time evolution of the radial average density difference for the optimized case. **f**, 1D-Simulation results without noise added to the potential.

describe similar noise characteristics as observed in the experiment. Figure 3.10c and f show the simulated density difference over time with and without noise on the potential. The desnity difference is again in arbitrary units, as it can not be directly compared to the 2D densities in the experiment. For the simulation with noise, a phenomenon similar to that in the experiment is observed: the wavepacket is partially scattered multiple times at the rough boundary, leading to incoherent reflection and destruction of the wavefront. Where, the atom number is still conserved. The effect of wavefront destruction due to multiple partial scatterings should be enhanced in 2D, as scattering can occur in more than just forward and backward direction. This is a possible explanation for why no coherent reflection is observed in the experiment. Scattering in directions other than the radial direction cannot be captured by the radial average analysis performed for the experimental results. How to deal with this challenge is discussed Section 3.3.1.

For the simulation without noise, the time evolution in the radial average closely matches the experimental results, supporting the hypothesis that noise is the relevant difference between the experiment and the simulation. Contrary to the simulation, the reflected wavepacket in the experiment is broader than the outgoing wavepacket. This discrepancy could be due to residual noise in the light potential, leading to scattering in polar direction, effectively broadening the wavepacket when multiple shots are averaged.

### 3.3.1. An Indicator for Reflectivity

Quantifying reflection on a rough surface, also known as diffuse reflection, is challenging. In the radial averaged analysis wave that are scattered in directions other than the radial direction could not be captured. Therefore, instead of looking at the radial average density difference over time, a straightforward approach is to track the standard deviation of the destiny difference $\langle \Delta\delta n(t) \rangle$ of the region where the condensate is flat. This metric is non-trivially related to the phonon number. If the density deviation $\langle \Delta\delta n(t) \rangle$ decreases after the wavepacket interacts with the boundary, it indicates a reduction in phonon number. However, this method does not capture any possible redistribution in the momentum space of the wavepacket.

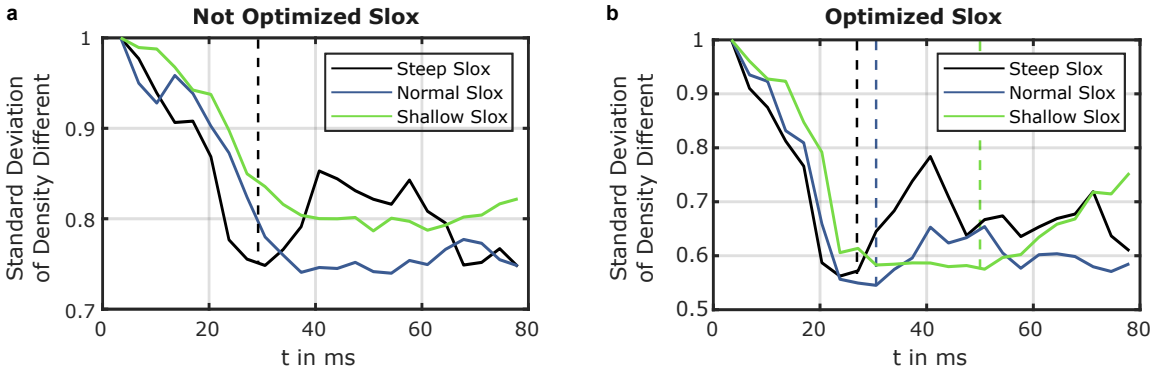



Figure 3.11: **Standard Deviation of the Density Difference as Indicator for Reflectivity. a**, The normalized standard deviation of the density difference $\langle \Delta\delta n(t) \rangle$ for the entire condensate over time, shown for a wavepacket evolution in the non-optimized steep, normal, and shallow slox potentials ($\beta = 14,\ 28,47\,\mathrm{Hz\,\mu m^{-1}}$). After reaching a minimum value when the wavepacket interacts with the boundary, $\langle \Delta\delta n(t) \rangle$ increases only for the steep slox ($t \sim 28\,\mathrm{ms}$), marked by the black dashed line. This indicates that only in the steep slox the wavepacket is reflected, in the non-optimized case. **b**, The density deviation $\langle \Delta\delta n(t) \rangle$ in the case of the optimized steep, normal, and shallow slox potentials. In this case, all three curves show a small increase after the wavepacket is reflected at the boundary ($t \sim 26,\ 32,50\,\mathrm{ms}$), demonstrating improved reflectivity due to optimization.

Figure 3.11a shows the normalized density deviation for wavepacket propagation in the non-optimized steep, normal, and shallow slox potentials ($\beta = 14,\ 28,47\,\mathrm{Hz\,\mu m^{-1}}$). The radial averages of the density differences over time for these measurements were already shown in Section 3.1. There, only the steep slox showed a reflected wavepacket. This is supported by the normalized density deviation: only the curve for the steep slox (black) increases again after the wavepacket is reflected at the boundary ($t = 28\,\mathrm{ms}$). While the curves for the normal (blue) and shallow (green) slox do not increase significantly after the wavepacket interacts with the boundary. Note that the wavepacket reaches the edge of the condensate at different times for each potential

Figure 3.11b shows the normalized density deviation for wavepacket propagation in the optimized steep, normal, and shallow slox potentials. The density distribution these three optimized slox are shown in Figure 3.12a. For all three cases, the density deviation shows an increase after reaching its minimum value at the time when the wavepacket is reflected at the boundary ($t \sim 26,\ 32,50\,\mathrm{ms}$). For the normal and shallow slox po-

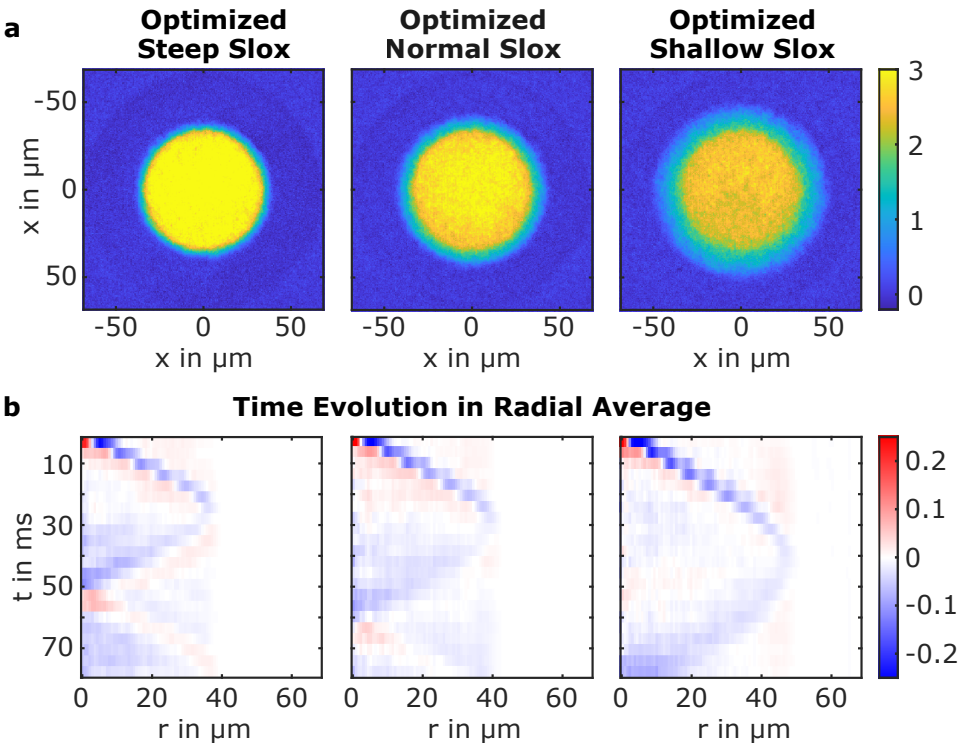



Figure 3.12: **Experimental Wavepacket Propagation in Slox Potentials with Different Slope. a**, Unperturbed density distribution for the optimized slox potentials with slopes of $\beta = 14,\ 28,47\,\mathrm{Hz\,\mu m^{-1}}$ (shallow, normal, steep slox). **b**, Wavepacket propagation in the corresponding potentials, visualized by the radially averaged density difference. For all three slox the wavepacket is reflected.

tentials the density deviation does not increases as much as for the steep slox but shows significant relative increases compared to their non-optimized counterparts. This is consistent with observations from the radial average density difference over time, shown in Figure 3.12b.

This indicator provides a useful means of comparing different boundary conditions as a first step. However, as noted earlier, it does not fully capture the complexity of the diffuse reflection process. Having identified that noise at the boundary plays a significant role in suppressing reflections, we now turn to engineering potentials to explicitly implement this as a strategy.

## 3.4. Artificial Noise in the Trapping Potential

It has been shown that the static noise in the light potential significantly influences the reflectivity of the boundary. To test which structural noise is best suited to implement absorptive boundaries, artificial noise was added to the slox potential. Directly adding the noise to the DMD without using the optimization algorithm would result in the pre-existing noise combined with the artificial noise, making it impossible to distinguish

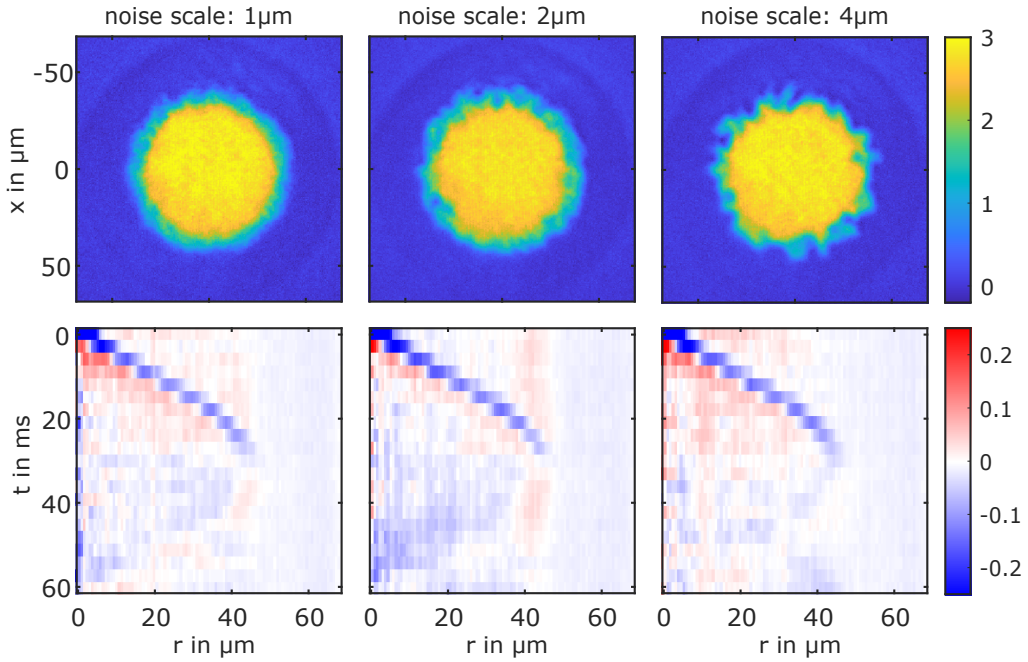



Figure 3.13: **Atom Densities and Wavepacket Propagation for Different Noise Scales on the Potential. Top Row:** Atom density with artificial noise applied to the light potential at different length scales. **Bottom Row:** Density difference $\delta n$ during the time evolution of a wavepacket in the corresponding trapping potentials. In all three cases, no reflection of the wavepacket is observed.

the effects of the two. Therefore, the optimization algorithm was used to optimize the light potential, so only the artificial noise and any residual noise left after optimization remain on the light potential.

The artificial noise was chosen analogously to that used in the simulations: pixel noise was added to the boundary and then smoothed using a Gaussian filter with a width $\sigma$. This approach ensures only noise on scales larger than the filter width remains. The atom densities for three different Gaussian filter widths are shown in Figure 3.13 (top row). The term noise scale denotes twice the width of the Gaussian filter, $2\sigma$. Here the slope of the slox is $\beta = 28\,\mathrm{Hz}\,\mu\mathrm{m}^{-1}$.

Figure 3.13 (bottom row) shows the radial averaged density difference during the time evolution of the wavepacket. For all three noise scales, no coherent reflection was absorbed. Moreover, no significant differences were observed between the three cases in the radial average. In the case of a noise scale of 1 µm, this is somewhat unexpected given that the atom density is relatively uniform and symmetric, indicating that even relatively minor noise scales significant effect the reflectivity. This suggests that a wavepacket may not be the optimal method to measure the impact of noise scale on the reflectivity, as a wavepacket is a superposition of waves with many different wavenumbers $k$. A method to test reflection for a specific $k$ by generating waves at a single wavenumber is presented in Section 4.

## 3.5. Hyperbolic Geometry for Absorptive Boundaries

A completely different idea to implement absorptive boundaries for phonons in the experiment, as well as the simulations is: If the wave never reaches the edge, it cannot be reflected. This idea was already mentioned in [35]. For this, we can calculate the time $T$ it takes a wave to travel to the edge of the condensate $\mathcal{R}$

$$T = \int_0^{\mathcal{R}} \frac{dr}{c_s(r)} \sim \int_0^{\mathcal{R}} \frac{dr}{\sqrt{n(r)}}. \tag{29}$$

At the edge, the local density, Thomas-Fermi, and Bogoliubov approximations fail, as the small excitations on top of the condensate become of the same order as the background density and the kinetic term in the GPE cannot be neglect anymore. Nonetheless, this is at least an indicator of how long a wave should take to reach the edge of the condensate. For the slox potential, the time $T$ is finite, and therefore reflection is expected. However, consider a density distribution like

$$n(r) = n_0 \left(1 - \frac{r^2}{\mathcal{R}^2}\right)^2, \tag{30}$$

the integral for the time $T$ diverges to infinity. This density is deeply connected to hyperbolic space, as explained in [26], but this connection will not be discussed further

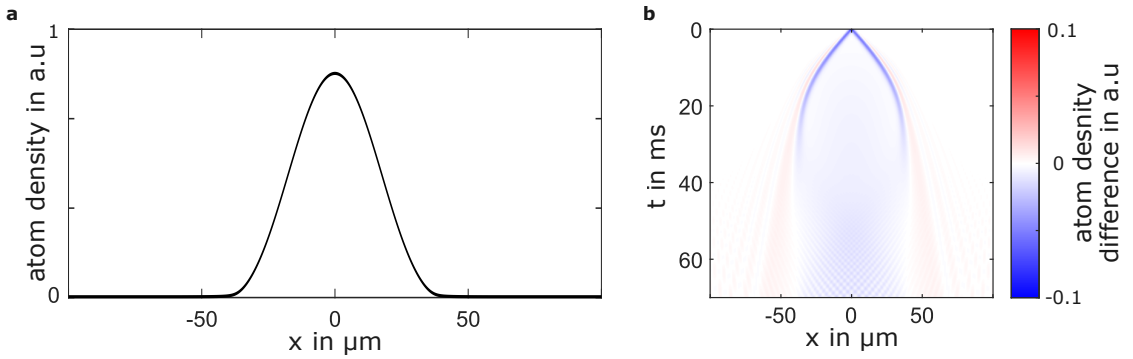



Figure 3.14: **Wavepacket Dynamics in a Hyperbolic Geometry. a**, Density distribution of the form $n(r) = n_0 \left(1 - (r/\mathcal{R})^2\right)^2$, theoretically leads to an infinite time it takes the wavepacket to travel to the edge of the condensate, thereby preventing reflection. **b**, 1D simulation of wavepacket dynamics in such a density distribution. The wavepacket slows down towards the edge and spreads out, but is not coherently reflected.

here. An advantage of such a density distribution is that the absorptiveness should not depend on noise in the light potential. Figure 3.14a shows a simulated ground state with such a density distribution. The density distribution was achieved by calculating the ground state for a potential of the form:

$$V(r) = V_0 \begin{cases} 1 - (1 - (r/\mathcal{R})^2)^2 & r < \mathcal{R}, \\ 1 & r \geq \mathcal{R}, \end{cases} \tag{31}$$

where the height of the potential $V_0$ is fine-tuned to match the chemical potential. The radius $\mathcal{R}$ is set to 40 µm.

Figure 3.14b shows the density difference during the time evolution of a wavepacket. As can be observed the wavepacket slows down towards the edge and then begins to spread out, but is not coherently reflected. This suggest that even for a perfectly smooth potential, a boundary that does not reflect can be created. The small wave pattern that can be seen at later in the middle of the density arise from high $k$ components in the wavepacket that travel faster than the speed of sound and get reflected at the simulation boundaries.

In order to implement this density in the experiment while accounting for noise in the light potential, it is necessary to use the iterative optimization algorithm. To perfectly account for noise in the light potential, the DMD and the CCD image of the atom cloud must be perfectly overlapped. While trying to optimize the atomic density for the hyperbolic density distribution, it was observed that this mapping was insufficient. Therefore the complicated boundary could not yet be implemented. The problem with the calibration of the mapping and a possible solution are presented in Appendix A.

# 4. Spontaneous Pattern Formation Analysis

If the interaction strength $g$ of the BEC is modulated periodically with a shaking frequency of $\omega_d$, a growth in the occupation of momentum with a certain resonant quasiparticles $k_r$ can be observed. At early times, this growth can be understood in terms of parametric resonances, and the production of pairs of quasiparticles with an energy of $\omega_d/2$ [36, 37, 38, 39], which corresponds to a certain resonant momenta $k_r$ determined by the Bogoliubov dispersion relation. At later times, with higher occupation, the stabilization of a square pattern is observed. This process depends on weak phonon-phonon interactions as is described in [10] and is theoretically explained under the assumption of an infinitely extended system in [40].

In this section, we will not delve into all the fascinating experiments that can be performed using this pattern. Instead, we will focus on how to quantify the occupation and correlation of the pattern (Section 4.1) in order to study the effect of the trapping potential on the pattern (Sections 4.2 and 4.3). A potential that suppresses coherent reflection of phonons is crucial for the emergence of a single pattern, because reflections lead to momenta that do not have the same orientation as the originating pattern, which interacts and destroys the spatial ordering. Therefore, these spontaneous pattern formation experiments are ideal for testing certain boundaries, directly benchmarking how well they mimic an infinitely extended system. Another advantage of these experiments is that only phonons with specific momentum are produced, in contrast to the broader spectrum produced by wavepackets. Additionally, the analysis of the pattern does not require radial averaging in real space, which averages out reflection effects in the polar direction, as it was done for the density difference for the wavepacket propagation.

## 4.1. Quantifying Occupations and Correlations of the Pattern

In the following experiment, the scattering length $a_s$, which is proportional to the interaction strength $g$, is modulated around a mean scattering length $\bar{a}_s$ of $200a_B$ with a drive frequency $\omega_d$ of 440 Hz and a relative amplitude $r$ of 0.3

$$a_s(t) = \bar{a}_s \left(1 - r \sin(\omega_d t)\right). \tag{32}$$

For this subsection the experiment has been performed in a slox potential with a slope of $\beta \sim 28\,\mathrm{Hz\,\mu m^{-1}}$ and radius of $R = 30\,\mu\mathrm{m}$. Figure 4.1 (top row) shows single shots of the atomic density distribution with a chemical potential of roughly 280 Hz, after 5, 15, 30, and 80 shaking periods, as well as an average density after 30 shake periods. At the beginning, randomly oriented stripes are produced by parametric resonance. The occupation of the resonant momentum $k_r$ grows exponentially (5 and 15 shake periods) without exhibiting a global structure. This can be seen in the density as excitations on a length scale of $2\pi/k_r \sim 8\,\mu\mathrm{m}$.

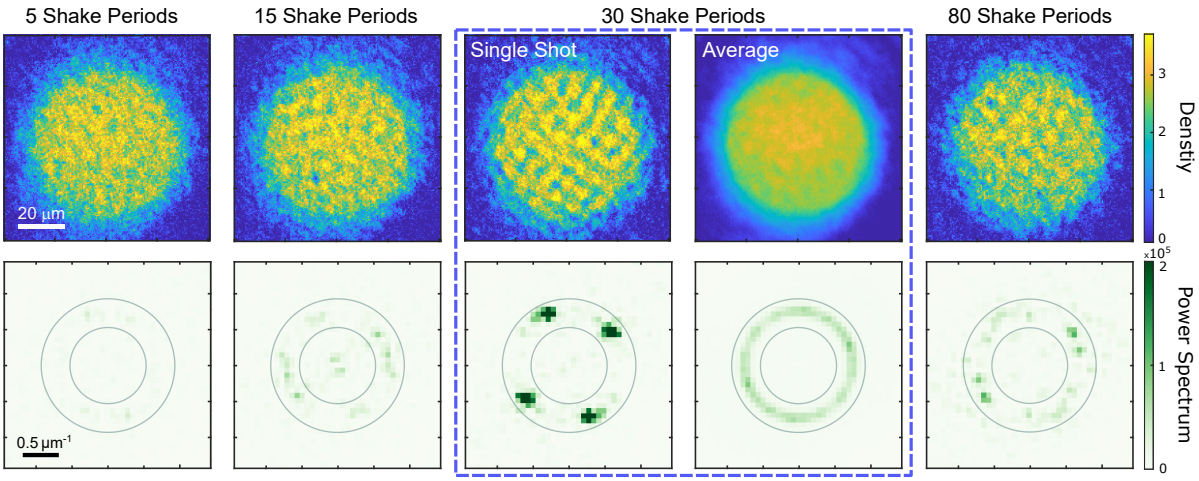



Figure 4.1: **Spontaneous Pattern Formation. Top Row:** Single shots of the density distribution after 5, 15, 30, and 80 shake periods, as well as the averaged density distribution of $\sim 30$ single shots after 30 shake periods. At early times, only randomly oriented stripes occur, which grow exponentially in occupation. After 30 shake periods, a square pattern stabilizes. The averaged density is again flat and radially symmetric, showing that the pattern occurs with random orientation and spatial phases. At later times, the pattern dissolves into unstructured density modulations. **Bottom Row:** Power spectrum of single shots after 5, 15, 30, and 80 shake periods, as well as the average of $\sim 30$ single power spectra after 30 shake periods. The growth of randomly oriented stripes can be seen as small occupations on the ring of resonant momentum $k_r$, indicated by the gray circles. After 30 shake periods, the square pattern can be seen in the power spectrum as four distinct peaks on the ring with 90° differences between them. The averaged power spectrum is a homogeneous ring, showing that the orientation of the pattern is random. At late times, the 90° correlation disappears, and other momenta besides $k_r$ become occupied. Figure adapted from Nikolas Liebster [10].

This can also be seen in the power spectrum of the single shots shown in the bottom row of Figure 4.1. Here, the power spectrum is defined as the Fourier transformed squared of the density contrast $\delta n_k = |\mathscr{F}(\delta n(\vec{x}))|^2$, with the density contrast is defined as $\delta n(\vec{x}) = n(\vec{x})/n_0(\vec{x}) - 1$, where $n_0(x)$ is the density without modulation of the scattering length. The density contrast is only evaluated in the flat part of the condensate. Randomly oriented stripes correspond to small peaks in a ring of resonant momenta $k_r$. The gray circles indicate the boundaries of the region used for further analysis.

After 30 shake periods, a square pattern can be observed in the single shots, corresponding to four peaks in the power spectrum, oriented on a ring with $\sim 90°$ between them. The density averaged over roughly 30 shots looks flat and radially symmetric again, and the averaged power spectrum shows a homogeneously filled ring. This shows that the

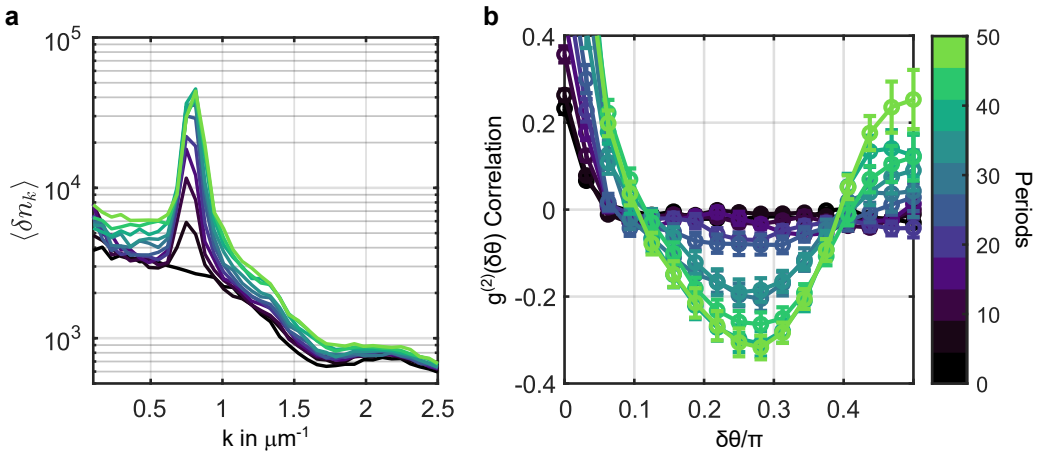



Figure 4.2: **Quantifying Occupation and Correlation of the Pattern. a**, Power spectrum averaged over the radial coordinate and roughly 30 realizations. A peak at the resonant momentum $k_r$ grows and then saturates. At later times, other momenta become occupied as well. **b**, Autocorrelation of the occupation along the ring $g^{(2)}(\delta\theta)$ over time. At early times, only random stripes are produced, which are uncorrelated, therefor only $g^{(2)}(\delta\theta) \neq 0$. At around 25 shake periods, the 90° correlation grows, while $\delta\theta = 45°$ becomes anticorrelated. This indicates that a single square pattern forms globally.

pattern forms with random orientations and random spatial phases. At later times, the global pattern in real space is destroyed, and no clear peaks with 90° difference are visible in the power spectrum. Instead, an increase in occupation at other momenta than the resonant $k_r$ is observed.

The aim is to quantify the pattern by analyzing the occupations and correlations on the ring in the power spectrum. Figure 4.2a shows the power spectrum averaged over the radial coordinate and roughly 30 realizations $\langle \delta n_k \rangle$. A clear peak at the resonant momentum $k_r$ grows and then saturates. At later times, momenta other than $k_r$ also become occupied. The value of $k_r$ is determined by fitting a parabola to the radially averaged power spectrum. In this case, it approximates to $k_r \sim 0.75\,\mu\text{m}^{-1}$. From this, the ring region for further analysis is defined as momenta within $k_r \pm 0.2\,\mu\text{m}^{-1}$. The occupation on this ring can then be tracked over time, defining the contrast of the pattern. To quantify the overall structure of the pattern, the ring is binned as a function of the polar angle $\theta$ into 32 bins, denoted by $\delta n_{k_r}(\theta)$. The autocorrelation of the occupation along the ring is calculated for each shot and averaged over all shots:

$$g^{(2)}(\delta\theta) = \left\langle \frac{\langle \delta n_{k_r}(\theta) \cdot \delta n_{k_r}(\theta + \delta\theta) \rangle_\theta}{\langle \delta n_{k_r}(\theta) \rangle_\theta^2} - 1 \right\rangle, \tag{33}$$

where $\langle ... \rangle_\theta$ denotes the average over all angles $\theta$, and $\langle ... \rangle$ denotes the average over all

shots. Figure 4.2b shows the correlation $g^{(2)}(\delta\theta)$ over time. At early times, only a peak at $\delta\theta = 0$ exists, which means no global structure in the condenstate is present. At roughly 25 shake periods, the correlation at $\delta\theta = 90°$ starts to grow, while $\delta\theta = 45°$ becomes anticorrelated. The 90° correlation corresponds to at least one square pattern forming, while anticorrelation at 45° indicates that only a single global square pattern is formed.

As mentioned earlier, for a single global pattern to grow and stabilize, it is important that boundaries do not coherently reflect the wave, as this leads to momenta that are not 90° correlated, interacting and destroying the pattern. Therefore, the correlation difference $g^{(2)}(\pi/2) - g^{(2)}(\pi/4)$ and the occupation on the ring $\langle \delta n_{k_r} \rangle$ as a function of the shake periods are good values to quantify the contrast and global structure of the pattern.

## 4.2. Effects of Different Potentials on Pattern Formation

To investigate the influence of boundary on pattern formation, the shaking experiment is performed for three different boundaries:

1. A box potential, which is essentially a steep slox potential with a very steep slope and a radius of 30 µm. The steepness is limited by the resolution of the objective (0.5 µm, at 532 nm), explained in Section 2.7.
2. A slox potential with a slope of $\beta \sim 28\,\mathrm{Hz\,\mu m^{-1}}$ and a radius of 30 µm.
3. The same slox potential, but with an optimized light potential.

In all three cases, the atoms are loaded identically into the traps. The box potential has a slightly higher averaged density in the center of the condensate and, therefore, a slightly higher chemical potential, because all atoms are located at $r < R$. This should, in the future, be accounted for by varying $R$ with $\beta$ such that the density in the center remains constant. However, this should not have a significant impact on the pattern formation, still allowing for the comparison of different potentials.

Figure 4.3a shows a single shot (left) and an average (right) of the density distribution after 45 periods for the box (upper row), slox (middle row), and the optimized slox (bottom row). For the box potential, no realization could be found where a global square pattern was observed. The density instead appears as randomly oriented stripes without a global structure. For both the slox and the optimized slox, shots where a square pattern emerges are shown. The pattern, however, looks less symmetric in the optimized slox case. This will be quantitatively analyzed by comparing the correlation. The averaged density distributions are smooth and symmetric in all three cases, showing that none of the potentials actively breaks the symmetry.

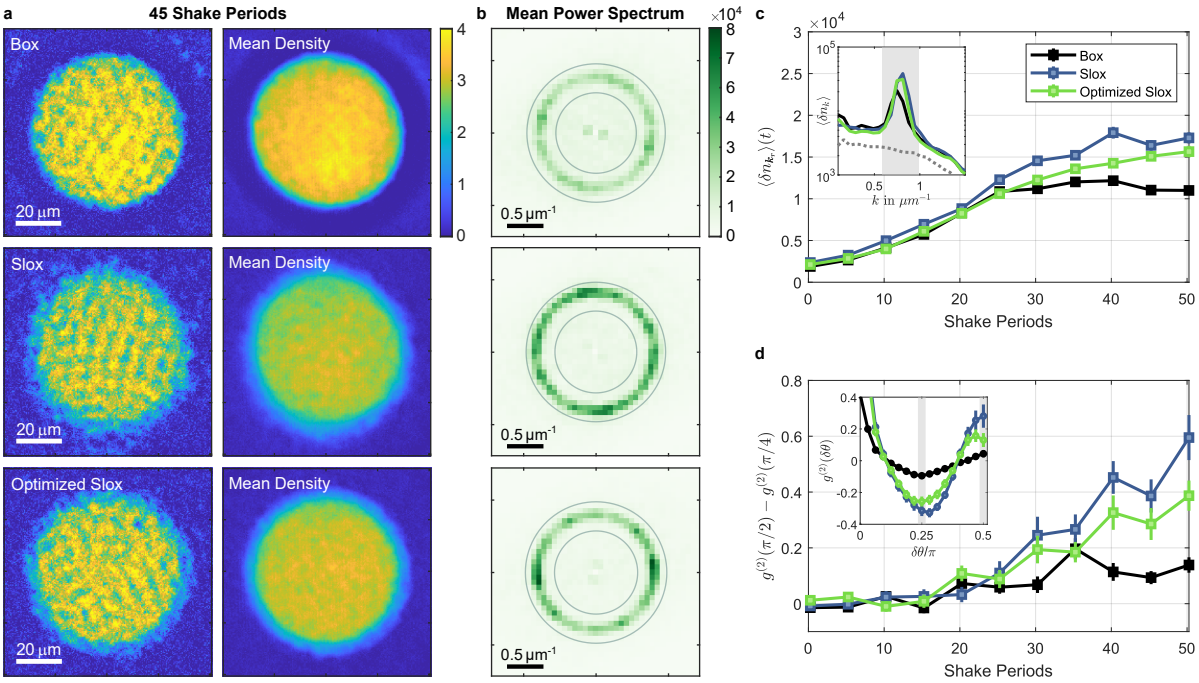



Figure 4.3: **Effects of Different Potentials on Pattern Formation.** **a**, Single shot (left side) and averaged atom density (right side) for the box (top row), slox (middle row), and optimized slox (bottom row) potentials. No global square pattern is visible in single shots for the box potential. The average in all three cases is smooth and symmetric. **b**, Power spectrum averaged over roughly 30 single spectra, showing a homogeneously filled ring at the resonant momenta $k_r$, indicated by the gray circles. **c**, Occupation of the ring over time. The inset shows the radially averaged power spectrum after 50 shaking periods, as well as without shaking for the slox potential for comparison, indicated by the gray dashed line. **d**, Correlation difference $g^{(2)}(\pi/2) - g^{(2)}(\pi/4)$ over time. The inset shows the full correlation function $g^{(2)}(\delta\theta)$ after 50 shaking periods. Figure adapted from [10].

Figure 4.3b shows the power spectrum averaged over all realizations, $\langle \delta n_k \rangle$. In all three cases, the ring at the resonant momenta $k_r$, indicated by the gray circles, is homogeneously filled. This shows again that the orientation of the pattern is random and that only one significant length scale is present. Slight inhomogeneities in the case of the optimized slox (bottom row) arise from limited statistics, as they cannot also be observed for other shaking periods.

The quantitative comparison of the occupations on the ring over time $\langle \delta n_{k_r} \rangle (t)$ are shown in Figure 4.3c. The inset shows the radially averaged power spectrum after 50 shaking periods. The gray dashed line depicts the initial radial averaged power spectrum without shaking for the slox potential. In all three cases, a clear peak at roughly

$0.75\,\mu m^{-1}$ is visible, along with homogeneous occupation at other momenta. The gray region indicates the range used for further analysis. For each potential, the resonant momenta $k_r$ were fitted individually, which may cause slight changes in the gray area between the three cases.

Figure 4.3d shows the difference between the 90° correlation and the 45° anti-correlation, $g^{(2)}(\pi/2) - g^{(2)}(\pi/4)$, over time. The inset depicts the full $g^{(2)}(\delta\theta)$ after 50 shaking periods. This has roughly the same form for all three potentials, i.e., correlation at 90° and anti-correlation at 45°, but with different amplitudes. At early times, the occupation on the ring grows exponentially with the same rate for all three potentials, while at the same time the correlation difference shows no structure. This is expected because, at early times, only randomly oriented stripes exist, and no patterns are present for the reflections to interact with. After about 25 shaking periods, the occupation curves for the box potential saturate, while still showing no increase in the correlation difference. At this time, the occupation of the optimized and non-optimized slox also starts to saturate but towards higher values. This is accompanied by a growing difference in the correlations at 90° and 45°. For both slox cases, the curves look similar, but the optimized slox consistently shows lower occupation and correlation differences.

Both the saturation of the occupation and the growth of 90° correlations start when the occupations reach a value where interactions between the randomly oriented stripes play a role and a single pattern is formed [10, 40]. This is also when reflections at the boundary start to play a role, because they can produce momenta oriented differently relative to the pattern, which than which interacts with the pattern and destroy the spatial ordering. Therefore, a global single pattern cannot exist in the case of the box potential, where reflections play a significant role. In case of the optimized slox the pattern formation is damped as reflections are enhanced relative to the not optimized slox. These results are consistent with the wavepacket analysis shown in Section 3, demonstrating that noise in the light potential significantly suppresses coherent reflections, thereby mimicking an infinitely extended system.

This also suggests that, rather than investigating the spontaneous formation of the pattern, one should investigate the lifetime of the pattern. The pattern can be imprinted by actively breaking the symmetry with the DMD and then stabilized by shaking [10]. This was not within the scope of this thesis and is a question for future research.

## 4.3. Pattern Formation for Different Noise Scales on the Potential

In this section, results for the shaking experiment, with different artificial noise on the boundary, are presented. The artificial noise was created as described in Section 3.4.

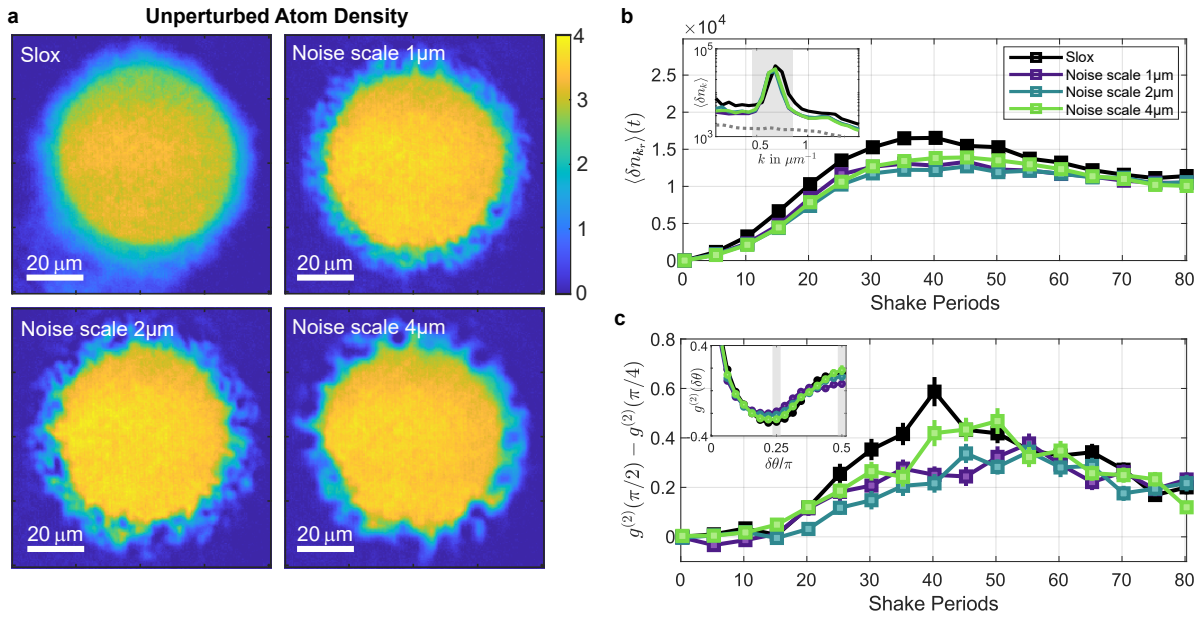



Figure 4.4: **Pattern Formation for Different Noise Scales on the Potential.** **a**, Density distributions for slox potentials with noise scales of 1, 2, 4 µm and a non-optimized slox potential for comparison. **b**, Occupation at the resonant momentum over time for three slox potentials with different noise scales 1, 2, 4 µm imprinted on them, as well as the non-optimized slox for comparison. The inset shows the radially averaged power spectrum after 50 shake periods, as well as before shaking for the slox potential for comparison (gray dashed line). **c**, Correlation difference $g^{(2)}(\pi/2) - g^{(2)}(\pi/4)$ over time. The inset shows the full correlation function $g^{(2)}(\delta\theta)$ after 50 shake periods.

The atom densities without shaking are shown in Figure 4.4a. An advantage of the spontaneously formed patterns compared to the wave packet analysis is that the reflectivity can be tested for the single resonant momentum $k_r$. This could be particularly interesting to study the interplay between the length scale of the excited momentum and the length scale of the noise.

Figure 4.4b shows the occupation in an analogous representation to Figure 4.3c for potentials with noise scales of 1, 2, 4 µm and a non-optimized slox potential for comparison. Again, only a single resonant momentum, which is similar for all four cases, is highly occupied (see inset in Figure 4.4b). The occupation again grows exponentially at early times, then shortly saturates before slowly decreasing. The occupation for all three potentials with artificial noise is roughly the same and slightly smaller than for the slox potential.

Figure 4.4b shows the correlation difference $g^{(2)}(\pi/2) - g^{(2)}(\pi/4)$ over time. The full correlation function $g^{(2)}(\delta\theta)$ after 50 shaking periods is depicted in the inset. For all

three cases, the correlation looks almost identical. The correlation difference over time again shows no structure until roughly 20 shaking periods, then increases, saturates, and decreases after about 50 shaking periods. For all three noise scales, the correlation difference is rather similar and slightly lower than for the slox potential in the time from 25 to 50 shake periods.

This shows that the artificial noise chosen does not further suppress the correct reflection but rather improves the reflections. The effect of different noise models needs to be studied further to determine which structural noise is best suited to implement an absorptive boundary, thereby creating an effectively infinitely extended system.

# 5. Conclusion and Outlook

This thesis investigated how phononic excitations in a quasi-two-dimensional Bose-Einstein Condensate get reflected on the confining potential boundaries. We especially considered a so-called slanted box (slox) potential, which is flat in the center and has linearly rising slopes at the edges. To probe the reflection of phonons on the system's boundary, wavepacket experiments have been performed in slox traps with differently sloped walls. The wavefront was only visibly reflected for very steep walls. To understand the underlying mechanism, we performed 1D-GPE simulations, where a wavepacket was prepared and propagated analogously to the experiment. Various wavepacket parameters, potential parameters, and other aspects of the simulation were investigated to reproduce the effect of suppressed reflection. This analysis showed that static spatial noise on the light potential leads to the destruction of the wavefront and any remaining reflection is faint and not coherent.

To validate this hypothesis experimentally, an iterative feedback algorithm was used to compensate any small imperfections in the light potential. This led to an enhanced coherent reflection of the wavepacket. Artificial noise was added to the light potential to test which structural noise is best suited to implement absorptive boundaries. However, the quality of the reflection didn't seem to depend on the length scale of the noise.

A different method to implement a boundary that does produces reflection was considered, using the concept of hyperbolic space. The idea is is to slowdown the wave asymptotically such that it never reaches the edge, and therefore cannot be reflected. While simulations showed exactly the intended effect, implementing this boundary in the experiment, using the new calibration method for the feedback algorithm remains a task for future work.

To put the new, absorbing boundaries to good use, the slox potential was tested by performing spontaneous pattern formation experiments. We investigated the emergence of spontaneously formed density patterns in an interaction-driven BEC. These experiments showed effect of the differently absorbing boundaries, which was quantified by looking at the occupation and correlation of the emergent patterns. These results also supported the hypothesis that suppression of coherent reflection arises from spatial noise on the light potential. It became apparent that the stability rather than the emergence of the pattern should be also considered. This is because, during early times of the exponential growth of the modes, the boundary has little impact, unlike at later times when the stability of the pattern is influenced by the boundary. Further investigation could determine if a certain noise scale is better suited to suppress coherent reflection.

The ability to mimic an infinitely extended system in a quantum simulator based using the slox potential could in the future be used for simulating different systems. For example, it will be interesting to see the effect in the simulation of bubble nucleation in a 2D spinor BEC [41], cosmological particle production in a 2D BEC [8, 29], or effects on the velocity field of a vortex [42].

# References


[1] Richard P Feynman. "Simulating physics with computers". In: *International Journal of Theoretical Physics* 21.6-7 (1982), pp. 467–488. DOI: 10.1007/BF02650179.

[2] M. Randeria, W. Zwerger, and M. Zwierlein. "The BCS-BEC crossover and the unitary fermi gas". In: *Lecture Notes in Physics* 836 (2012), pp. 1–. DOI: 10.1007/978-3-642-21978-8_1.

[3] M. Holten et al. "Observation of Cooper pairs in a mesoscopic two-dimensional Fermi gas". In: *Nature* 606 (2022), pp. 287–291. DOI: 10.1038/s41586-022-04678-1.

[4] Waseem S. Bakr et al. "A quantum gas microscope for detecting single atoms in a Hubbard-regime optical lattice". In: *Nature* 462 (2009), pp. 74–77. DOI: 10.1038/nature08482.

[5] Jacob F. Sherson et al. "Single-atom-resolved fluorescence imaging of an atomic Mott insulator". In: *Nature* 467 (2010), pp. 68–72. DOI: 10.1038/nature09378.

[6] Antoine Browaeys and Thierry Lahaye. "Many-Body Physics with Individually-Controlled Rydberg Atoms". In: *Nature Physics* 16 (2020), pp. 1–11. DOI: 10.1038/s41567-019-0733-z.

[7] Loïc Henriet et al. "Quantum computing with neutral atoms". In: *Quantum* 4 (2020), p. 327. ISSN: 2521-327X. DOI: 10.22331/q-2020-09-21-327.

[8] C. Viermann, M. Sparn, N. Liebster, et al. "Quantum field simulator for dynamics in curved spacetime". In: *Nature* 611 (2022), pp. 260–264. DOI: 10.1038/s41586-022-05313-9.

[9] Marius Sparn et al. "Experimental particle production in time-dependent spacetimes: A one-dimensional scattering problem". In: *Physical Review Letters* (2024). Accepted 15 November 2024.

[10] Nikolas Liebster et al. *Emergence of crystalline steady state in a driven superfluid.* 2023. arXiv: 2309.03792 [cond-mat.quant-gas].

[11] Nikolas Liebster et al. "Observation of supersolid sound modes in a driven quantum gas". In preparation. 2024.

[12] Maurus Hans et al. "Bose-Einstein condensate experiment as a nonlinear block of a machine learning pipeline". In: *Phys. Rev. Res.* 6 (1 2024), p. 013122. DOI: 10.1103/PhysRevResearch.6.013122.

[13] Sandro Stringari Lev Pitaevskii. *Bose–Einstein Condensation and Superfluidity.* Vol. 1. 2016.

[14] E. P. Gross. "Structure of a quantized vortex in boson systems". In: *Nuovo Cimento* 20 (1961), pp. 454–477. DOI: 10.1007/BF02731494.

[15] L. P. Pitaevskii. "Vortex Lines in an Imperfect Bose Gas". In: *Journal of Experimental and Theoretical Physics* 13 (1961), pp. 451–454.

[16] N. N. Bogolyubov. "On a New method in the theory of superconductivity". In: *Nuovo Cim.* 7 (1958), pp. 794–805. DOI: 10.1007/BF02745585.

[17] A. Marte et al. "Feshbach Resonances in Rubidium 87: Precision Measurement and Analysis". In: *Phys. Rev. Lett.* 89 (28 2002), p. 283202. DOI: 10.1103/PhysRevLett.89.283202.

[18] M. W. Zwierlein et al. "Observation of Bose-Einstein Condensation of Molecules". In: *Phys. Rev. Lett.* 91 (25 2003), p. 250401. DOI: 10.1103/PhysRevLett.91.250401.

[19] Eike Nicklas. "A new tool for miscibility control: Linear coupling". PhD Thesis. Heidelberg University, 2013.

[20] L. Salasnich, A. Parola, and L. Reatto. "Effective wave equations for the dynamics of cigar-shaped and disk-shaped Bose condensates". In: *Phys. Rev. A* 65 (4 2002), p. 043614. DOI: 10.1103/PhysRevA.65.043614.

[21] Weizhu Bao and Yongyong Cai. "Mathematical theory and numerical methods for Bose-Einstein condensation". In: *Kinetic and Related Models* 6.1 (2013), pp. 1–135. ISSN: 1937-5093. DOI: 10.3934/krm.2013.6.1.

[22] M.D Feit, J.A Fleck, and A Steiger. "Solution of the Schrödinger equation by a spectral method". In: *Journal of Computational Physics* 47.3 (1982), pp. 412–433. ISSN: 0021-9991. DOI: https://doi.org/10.1016/0021-9991(82)90091-2.

[23] Juha Javanainen and Janne Ruostekoski. "Symbolic calculation in development of algorithms: split-step methods for the Gross–Pitaevskii equation". In: *Journal of Physics A: Mathematical and General* 39.12 (2006), p. L179. DOI: 10.1088/0305-4470/39/12/L02.

[24] "Optical Dipole Traps for Neutral Atoms". In: ed. by Benjamin Bederson and Herbert Walther. Vol. 42. Advances In Atomic, Molecular, and Optical Physics. Academic Press, 2000, pp. 95–170. DOI: https://doi.org/10.1016/S1049-250X(08)60186-X.

[25] Maurus Hans. "Physical Computing on a Versatile Setup for Ultra-cold Potassium". PhD Thesis. Heidelberg University, 2022.

[26] Celia Viermann. "Cosmological particle production and curced spaces in an ultracold quantum gas". PhD Thesis. Heidelberg University, 2022.

[27] Jiří Etrych et al. "Pinpointing Feshbach resonances and testing Efimov universalities in $^{39}$K". In: *Phys. Rev. Res.* 5 (1 2023), p. 013174. DOI: 10.1103/PhysRevResearch.5.013174.

[28] Marcel Kern. "Enhanced Local Control of Two-Dimensional Ultracold Atomic Clouds". Master Thesis. Heidelberg University, 2024.

[29] Mireia Tolosa-Simeón et al. "Curved and expanding spacetime geometries in Bose-Einstein condensates". In: *Phys. Rev. A* 106 (3 2022), p. 033313. DOI: 10.1103/PhysRevA.106.033313.

[30] Michele Sciacca and Nicholas Parker. "Matter-wave dark solitons in box-like traps". In: *Physical Review A* 95 (2017), p. 013628. DOI: 10.1103/PhysRevA.95.013628.

[31] Jens Philipp Ronzheimer. "Interactions of Dark Solitons in cigar shaped Bose-Einstein Condensates". PhD Thesis. Heidelberg University, 2008.

[32] Th. Busch and J. R. Anglin. "Motion of Dark Solitons in Trapped Bose-Einstein Condensates". In: *Phys. Rev. Lett.* 84 (11 2000), pp. 2298–2301. DOI: 10.1103/PhysRevLett.84.2298.

[33] Eniko J. M. Madarassy. *Decay of soliton-like perturbations into vortex - anti vortex pairs*. 2009. arXiv: 0807.3893 [cond-mat.other].

[34] P. Blair Blakie et al. "Dynamics and statistical mechanics of ultra-cold Bose gases using c-field techniques". In: *Advances in Physics* 57 (2008), pp. 363–455. URL: https://api.semanticscholar.org/CorpusID:14999178.

[35] Mohammadamin Tajik et al. "Experimental observation of curved light-cones in a quantum field simulator". In: *Proceedings of the National Academy of Sciences* 120.21 (2023), e2301287120. DOI: 10.1073/pnas.2301287120.

[36] M. Faraday. "On a peculiar class of acoustical figures; and on certain forms assumed by groups of particles upon vibrating elastic surfaces". In: *Philosophical Transactions of the Royal Society of London* 3 (1837), p. 49.

[37] K. Staliunas, S. Longhi, and G. J. de Valcárcel. "Faraday patterns in Bose-Einstein condensates". In: *Physical Review Letters* 89 (2002), p. 210406.

[38] I. Carusotto et al. "Density correlations and analog dynamical Casimir emission of Bogoliubov phonons in modulated atomic Bose-Einstein condensates". In: *The European Physical Journal D* 56 (2010), p. 391.

[39] X. Busch, R. Parentani, and S. Robertson. "Quantum entanglement due to a modulated dynamical Casimir effect". In: *Physical Review A* 89 (2014), p. 063606.

[40] Keisuke Fujii et al. "Stable-fixed-point description of square-pattern formation in driven two-dimensional Bose-Einstein condensates". In: *Phys. Rev. A* 109 (5 2024), p. L051301. DOI: 10.1103/PhysRevA.109.L051301.

[41] Thomas P Billam, Kate Brown, and Ian G Moss. "Bubble nucleation in a cold spin 1 gas". In: *New Journal of Physics* 25.4 (2023), p. 043028. DOI: 10.1088/1367-2630/accca2.

[42] Sang Seo et al. "Observation of vortex-Antivortex pairing in decaying 2D turbulence of a superfluid gas". In: *Scientific Reports* 7 (2017). DOI: 10.1038/s41598-017-04122-9.

[43] MathWorks. *Matlab function fitgeotform2d*. https://de.mathworks.com/help/images/ref/fitgeotform2d.html. Accessed: 19-Oct-2024.

[44] T. G. Tiecke. *Properties of potassium*. 2011.

[45] Charbel Cherfan et al. "Multi-frequency telecom fibered laser system for potassium laser cooling". In: *Applied Physics Letters* 119.20 (2021), p. 204001. ISSN: 0003-6951. DOI: 10.1063/5.0070646.

[46] Pure Photonics. *Pure Photonics - Support*. https://purephotonics.com/support/. Accessed: 16-Sep-2024.

[47] Keopsys by Lumibird. *EDFA Data Sheet*. http://www.keopsys.com/portfolio/cw-erbium-fiber-amplifier-c-bo-hp-series/. Accessed: 11-Oct-2024.

[48] HC Photonics. *PPLN Crystal Operation Principle*. https://www.hcphotonics.com/ppln-chips. Accessed: 11-Oct-2024.

# Appendix A New Calibration Method for Light Potential Optimization Algorithm

As explained in Section 2.7, the DMD can in principle be used to project arbitrary light potentials onto the atom plane. The atom plane is then imaged using absorption imaging. To optimize the light potential with the previously mentioned iterative optimization algorithm, individual mirrors must be flipped to locally adjust the potential, resulting in increase or decrease of atoms at these specific positions. For this, the images of the atom plane and the DMD plane must be mapped onto each other.

Previously, this calibration was performed by imprinting three holes in the condensate at three different positions using the DMD. The density distribution with holes is shown in Figure A.1a. The positions of these holes on the camera image of the condensate are extracted by fitting a two-dimensional Gaussian profile to each of them. A triangle is created for both the positions of the holes in the atom plane and the DMD plane, as shown in Figure A.1b. These triangles are then overlapped using a similarity transformation, as illustrated in Figure A.1c. This calibration is described in detail in [28]. This transformation allows for translation in the $x$- and $y$-directions ($t_{x,y}$), rotation by an angle $\theta$, and a global scaling by $s$.

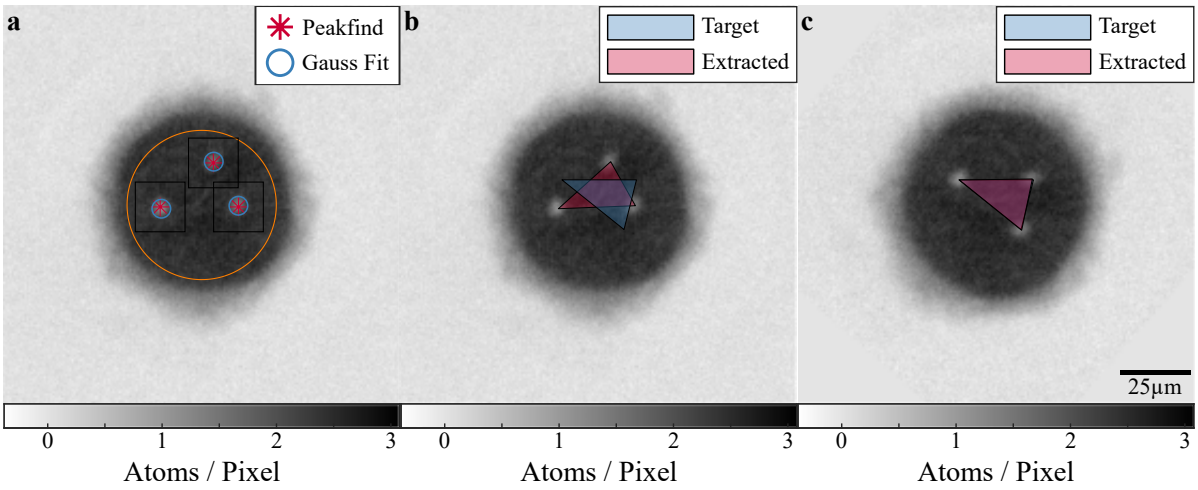



Figure A.1: **Previous DMD Calibration. a**, Extraction of the position of the holes in the condensate by fitting a two-dimensional Gaussian profile. The approximate positions of the holes are determined using a peak-finding algorithm within 2/3 of the condensate radius, indicated by the orange ring. **b**, Triangles are created for the positions on the DMD (blue) and the extracted positions on the camera (red). **c**, Overlapping triangles after applying a similarity transformation. Figure taken from Marcel Kern [28].

While attempting to optimize the light potential for the hyperbolic atom density mentioned in Section 3.5, it was observed that the atom density was not perfectly radially symmetric but slightly egg-shaped, even though the DMD configuration was radially symmetric. This phenomenon could arise from small tilts between the DMD plane, the atom plane, and the camera plane, caused by slight misalignments (e.g the camera or DMD not being perfectly parallel to the atom plane in the experiment). With such tilts, a similarity transformation with a single scaling parameter $s$ is insufficient to map the camera image onto the DMD plane. Therefore, the optimization algorithm can not work, especially toward the edge of the condensate or for more complex trap geometries. This effect had not been observed while optimizing the slox potential, probably because the trap geometry is smooth and does not contain sharps jumps.

The idea for the new calibration method is to use an affine transformation. This transformation can allows for translation in the $x$- and $y$-directions, rotation, scaling in $x$ and $y$, and shear in $x$ and $y$. The general form of the transformation matrix is

$$\mathbf{T} = \begin{pmatrix} \cos\theta & \sin\theta & 0 \\ -\sin\theta & \cos\theta & 0 \\ 0 & 0 & 1 \end{pmatrix} \begin{pmatrix} s_x & 0 & 0 \\ 0 & s_y & 0 \\ 0 & 0 & 1 \end{pmatrix} \begin{pmatrix} 1 & 0 & 0 \\ \alpha_y & 1 & 0 \\ 0 & 0 & 1 \end{pmatrix} \begin{pmatrix} 1 & \alpha_x & 0 \\ 0 & 1 & 0 \\ 0 & 0 & 1 \end{pmatrix} \begin{pmatrix} 1 & 0 & 0 \\ 0 & 1 & 0 \\ t_x & t_y & 1 \end{pmatrix}, \quad (34)$$

where $\theta$ is the rotation angle, $s_{x,y}$ are the scaling factors, $\alpha_{x,y}$ are the shear factors, and $t_{x,y}$ are the translations in the $x$- and $y$-directions. This matrix is then applied to each pixel of the images, which can be written as $(x, y, 1)$. How each of these parameters influences the transformed image is schematically illustrated using a checkerboard pattern in Figure A.2a to d. The Figure A.2e shows how a nonlinear transformation would influences the image. In comparison to the previous transformation, the new approach allows $\alpha_{x,y} \neq 0$ and $s_x \neq s_y$. For this more complex transformation, a minimum of three points is required to make the transformation unique. However, including more points decreases the uncertainty of the transformation parameters.

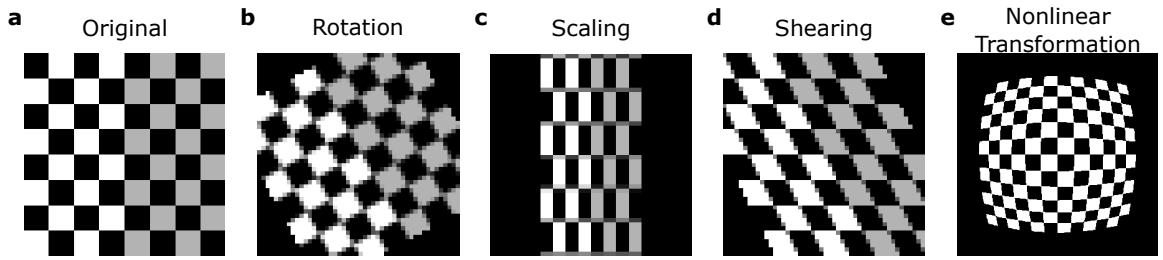



Figure A.2: **Schematic Illustration of Affine Transformation Effects. a**, Original image. **b,c,d** Schematic illustration of how rotation, scaling, and shearing transformations affect the checkerboard pattern. **e**, Schematic illustration of how a nonlinear transformation, which is not included in the affine transformation, affects the checkerboard pattern.

## A.1 Is a Linear Transformation Enough?

First, it can be shown that a linear global transformation is sufficient by verifying that rings with linearly increasing radii in the DMD plane also produce rings with linearly increasing radii in the atom plane. To demonstrate this, rings with radii of 0, 150, 300, 450, and 600 DMD pixels were imprinted on the atoms. It should be noted that 600 pixels correspond to $\sim 53\,\mu m$ in the atom plane, which is larger than the usual atom cloud size. Figure A.3a shows the corresponding image of the atoms. The density decreases toward the edge due to a broad harmonic trap confining the atoms.

Figure A.3b shows the radial average of this atom density. The positions of the minima in the radial density, i.e., the radii of the circles in the atom plane, are extracted by locally fitting a parabolic function of the form $f(x) = a \cdot (x - b)^2 + c$. The radii in the atom plane and the corresponding radii in the DMD plane are plotted in Figure A.3c. The last ring couldn't fitted properly, and for the first three rings the relationship is linear, proving that a linear transformation is sufficient to map the atom plane to the DMD plane. The gray dashed line indicated the typical size of the atom cloud.

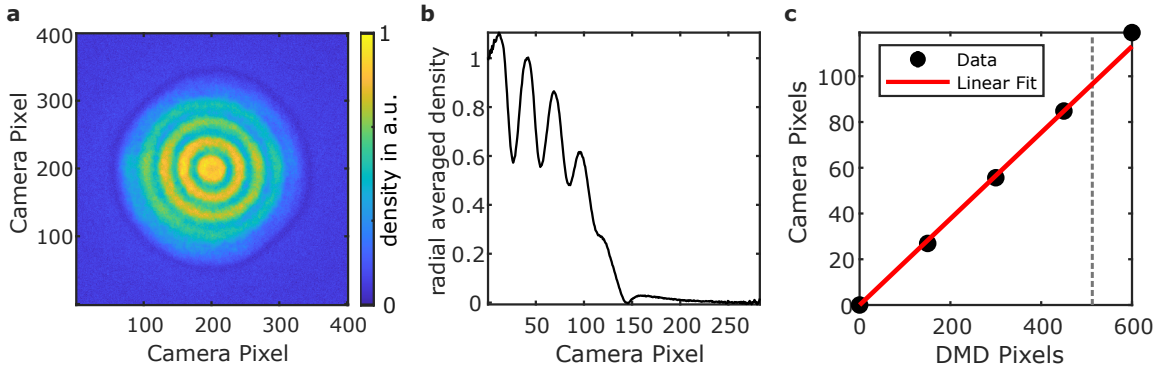



Figure A.3: **Rings in the Atom Plane. a**, Rings with radii of 0, 150, 300, 450, and 600 DMD pixels are imprinted on the atoms. **b**, Radial average of the atom density. This allows for the extraction of the radii of the rings in camera pixels via a local parabolic fit. **c**, The radii in camera pixels and the corresponding radii in DMD pixels show a linear dependency. The gray dashed line indicated the typical size of the atom cloud.

## A.2 Affine Transformation

The calibration using an affine transformation works similarly to the previous method. However, instead of three holes, five are used to enhance the certainty of the transformation parameters. The algorithm that detects and measures the positions of the holes in the condensate does not generally label the holes in the same order as their positions on the DMD. However, each point in the atom plane must be transformed to the corresponding point on the DMD. To solve this problem, the holes are chosen such that

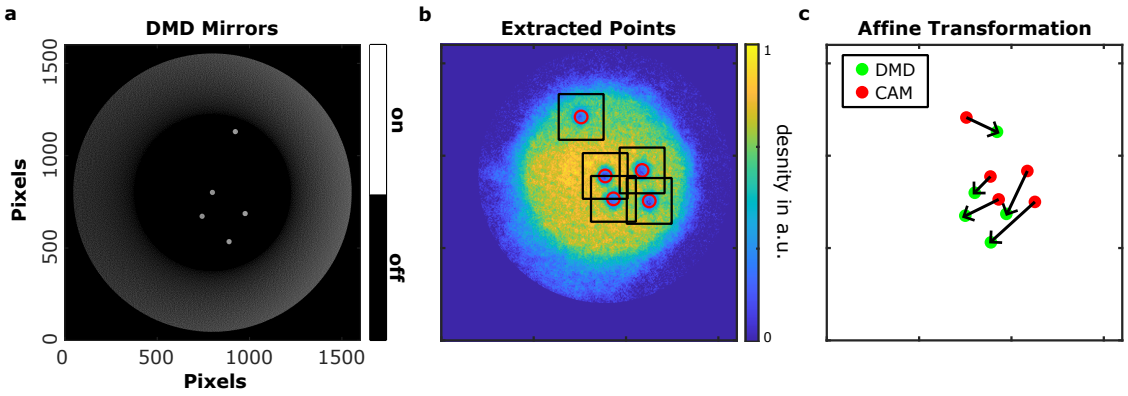



Figure A.4: **Affine Transformation for DMD Calibration. a**, DMD mirror configuration to produce five holes in the atom plane. **b**, Atom density with five holes inside. The black rectangle marks the area where a 2D Gaussian fit is applied to extract the positions of the holes. The red circle indicate the width of the Gaussian fit. **c**, Points in the DMD plane are shown in green, and the extracted points in the camera image are shown in red. The black arrows depict how the affine transformation is applied to the points in the camera image.

they are equidistantly spaced from their center of mass, allowing the positions on the DMD and the atom plane to be sorted in the same order. It should be noted that this method only works if the tilt is sufficiently small. Then, the built-in MATLAB function `fitgeotform2d` is used to calculate the transformation matrix [43].

Figure A.4a shows the mirror configuration of the DMD. The atoms are confined with a slox potential, and the five holes for calibration are imprinted by turning on roughly 20% of the mirrors in a circle with a radius of 15 pixels. The camera image of the corresponding condensate is prescaled by $s = 5.5$ and shifted such that the atom cloud is in the center of the image. The image is then interpolated to a resolution of $1600 \times 1600$ pixels to match the size of the DMD. This pretransformed image is shown in Figure A.4b. The pretransformation parameters are fixed and applied to the images for optimization before the affine transformation is applied. The black rectangles mark the regions where a two-dimensional Gaussian fit is performed to extract the precise positions of the holes in the condensate. The red circles indicate the width of the fitted Gaussian profiles.
Figure A.4c shows the extracted positions of the holes in the camera image (red) and in the DMD plane (green). The black arrows show the transformation applied to the points in the atom plane. As can be observed, these transformed points almost perfectly map to the points in the DMD plane. The calculated transformation parameters for our experiment are $\theta = 42.06°$, $s_x = 1.062$, $s_y = 0.992$, $\alpha_x = 0.0136$, $\alpha_y = 0$, $t_x = 724.50$, and $t_y = -316.74$. The shear $\alpha_x$ corresponds to a shear angle of 0.78°. The shifts in the $x$- and $y$-directions are large because the rotation around $(x, y) = (0, 0)$ (bottom left of the image) is applied before the translation.

It could be shown that different scaling factors in $x$ and $y$ are indeed required. The shear, however, is small but it is still accounted for by the new calibration method. Within the scope of this thesis, the new calibration method has not yet been used to calibrate the light potential and will be a task for future work.

# Appendix B New Laser for the Potassium D1- and D2-Lines

For laser cooling of potassium-39, a laser resonant with the $2S_{1/2}$ to $2P_{1/2}$ transition, also known as the D1-line (770.108 nm), and a laser resonant with the $2S_{1/2}$ to $2P_{3/2}$ transition, also known as the D2-line (766.701 nm) [44], is needed. Sufficient power is required to ensure a stabile cooling process over extended periods. A laser resonant with the D-lines of $^{39}$K can, in principle, also be used to cool potassium-41, as the lines differ by only about 235 MHz between the isotopes, as can be seen in the level scheme for $^{39}$K and $^{41}$K shown in Figure B.1. This frequency difference can be achieved using an acousto-optic modulator (AOM). For efficient cooling, the power, polarization, and frequency must be controlled and stabilized. The natural linewidth of these transitions is $\Gamma/2\pi \approx 6$ MHz [44], and thus the frequency of the cooling lasers must be more stable than this linewidth.

In the current experiment, a laser from TOPTICA (DL PRO) is used for the D1-line, which is amplified with two consecutive tapered amplifiers (TAs). With this setup, about 450 mW of power is achieved. Some aspects that could be improved with a different more reliable setup include wear and tear of the TAs over time, the need for frequent recoupling, occasional loss of frequency stabilization, and the potential for achieving higher power.

We benefit from the fact that the D1- and D2-lines are in the region of half the wavelength of typical telecommunication wavelengths (1270 nm to 1610 nm). This enables the use of highly reliable and cost-effective telecommunication hardware, together with second harmonic generation (SHG), to achieve a more stable, powerful, and versatile laser at the desired wavelengths. Another advantage is that telecommunication hardware is fiber-based and therefore the laser setup is expected to be more stabile. In the following, such a laser setup is presented and characterized. The design and concept are inspired by the work of Charbel et al. [45].

The basic idea of the laser is to use a seed laser that is amplified by an Erbium-doped fiber amplifier (EDFA) and then frequency doubled in a nonlinear crystal. These three main components will be explained in Section B.1. The SHG optimization will be discussed in Section B.2. In Section B.3, the frequency stabilization using Doppler-free absorption spectroscopy of potassium is presented and characterized. Section B.4 discusses the current status and future plans for the laser.

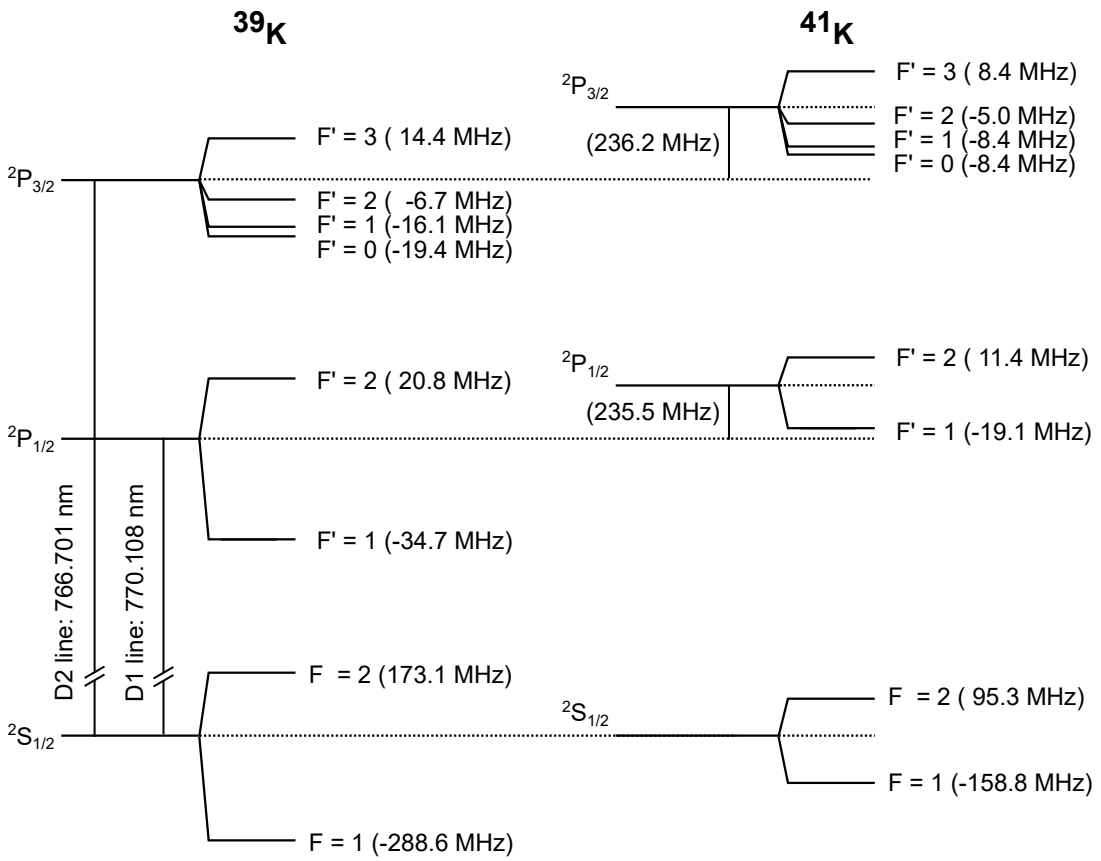



Figure B.1: **Level Scheme of $^{39}$K and $^{41}$K.** The transitions from the ground state $2S_{1/2}$ to the excited states $2P_{1/2}$ and $2P_{3/2}$ are known as the D1- and D2-lines. The D-lines for $^{41}$K differ by only about 235 MHz compared to those of $^{39}$K. Figure adapted from [26] and values taken from [44].

## B.1 The Main Components: Seed, Amplifier, SHG Crystal

For the seed laser, the external-cavity diode laser (ECDL) PPCL550 from PurePhotonics is used. The laser is specified to have a power range of 4 mW to 25 mW, a center wavelength of 1528 nm to 1565 nm, a linewidth of 10 kHz, linear polarization, and a fiber-based output coupler [46]. The laser offers two options for frequency modulation (FM): a fast FM using a piezoelectric crystal with a modulation frequency of up to 100 kHz and a range of ±50 MHz, and a slow thermal FM with a range of ±30 GHz and a maximum tuning rate of 125 MHz s$^{-1}$. The internal laser stability is specified to deviate by no more than 40 MHz over 1 s. The seed laser is coupled to an optical fiber-based Faraday isolator (ISO) to prevent unwanted back reflections into the laser. The design and specifications for the seed laser are all contained in the data sheet, which is openly accessible at [46]. Instructions on how to communicate with the laser are described in Appendix B.7.
The seed light is fiber-coupled into the Erbium-doped fiber amplifier (EDFA) CEFA-

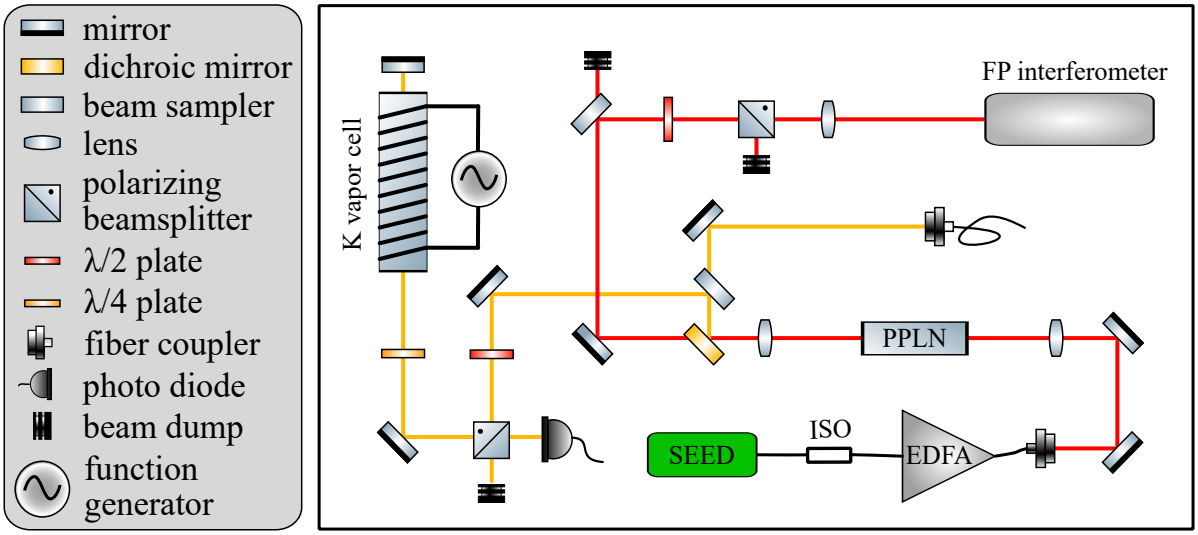



Figure B.2: **Schematics of the Laser Letup.** A 10 mW seed at 1540 nm is amplified to a maximum of 12 W using an EDFA. This pump beam is focused into a PPLN crystal for SHG. The SHG beam has a power of 1.5 W and is split from the pump beam using a dichroic mirror. A small portion of the pump power is coupled into a Fabry–Pérot interferometer. About 1 mW of the SHG light is picked off for Doppler-free absorption spectroscopy, and the rest is coupled into a fiber for cooling.

C-PB-HP from LUMIBIRD [47]. This amplifier is designed for wavelengths of $(1533.0 \pm 1.5)$ nm and $(1540.0 \pm 1.5)$ nm with a maximum output power of 12 W. The measured output power versus the EDFA current is plotted in Figure B.3 a), along with a linear fit.

The crystal used for SHG is a 5 cm long periodically poled lithium niobate (PPLN) crystal from HCP. The PPLN operates by quasi-phase-matching; therefore, the grating must be chosen correctly for the desired wavelength [48]. This PPLN has multiple grating aligned in parallel along the long axis of the crystal. The gratings are optimized for frequencies between 1510 nm and 1630 nm. To achieve high efficiency, the grating needs to be fine-tuned by adjusting the crystal's temperature.

## B.2 SHG Setup

The schematic laser setup is shown in Figure B.2, and all components can be found in Section B.5. After amplification of the seed light, a fiber out-coupler is used to create a collimated free-space beam with a diameter of approximately 1.9 mm. Using two mirrors and a lens (f = 150 mm), the beam is focused down to a focal waist of 160 µm inside the PPLN crystal. For an efficient SHG process, a stable and precise temperature is required. This is achieved with the TC038D oven from HCP. The optimal temperature for the D1-line was found to be $(119.4 \pm 0.1)$ °C. This temperature is linearly dependent

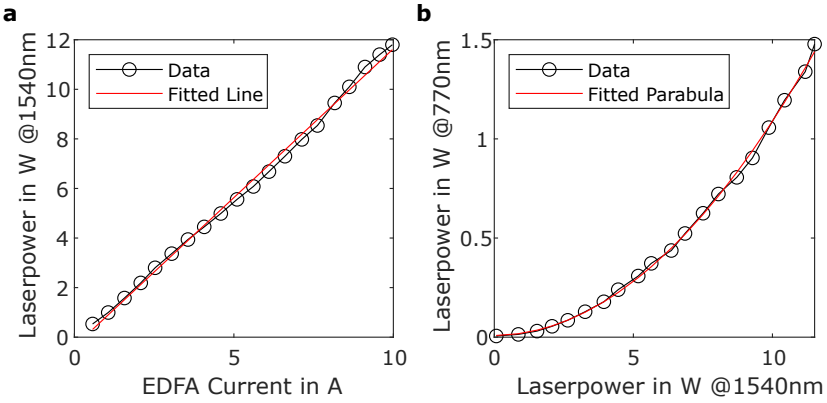



Figure B.3: **Pump and SHG Power. a**, EDFA laser power at 1540 nm as a function of EDFA current, together with a linear fit. **b**, SHG power at 770 nm as a function of pump power at 1540 nm, together with a parabolic fit. The maximum achieved SHG power is 1.5 W, which corresponds to a conversion efficiency of 12.5 %.

on the wavelength with a slope of $0.14\,\mathrm{nm}\,^{\circ}\mathrm{C}^{-1}$. To find the correct temperature, the oven is heated to around 200 °C then turned off, allowing it to slowly cool down while monitoring the SHG power.

Figure B.3 b) shows the measured SHG power (before the fiber) versus the pump power, along with a parabolic fit. The maximum achieved conversion efficiency is 12.5 %, corresponding to an SHG power of 1.5 W. This is comparable to the conversion efficiency and power achieved by Charbel et al. [45].

After the crystal, a second lens (f = 150 mm at 770 nm) is used to collimate the SHG beam. Due to the nonlinear effects of the SHG process, the diameter of the SHG beam is now $(1.1 \pm 0.1)\,\mathrm{mm}$, which is approximately $1/\sqrt{2}$ of the pump beam diameter. A dichroic mirror is used to separate the pump and SHG beams. A small portion of the pump power is coupled into the FPI. The FPI is used to check if the laser is multi-mode. The power stability was measured to have a standard deviation of 0.4 % at an SHG power of 1.5 W over one minute, with only a shift of 0.03 % over 24 hours. When not frequency-locked, the laser exhibited a drift of approximately 1.2 GHz over a period of 24 hours. No changes in polarization were observed during this period.

## B.3 Frequency Stabilization on Potassium Absorption Lines

While most of the SHG light is coupled into a fiber for use in the experiment, a small portion (approximately 1 mW) is picked off using a beam sampler and used for Doppler-free absorption spectroscopy. The basic principle of Doppler-free absorption spectroscopy is passing the beam through a cell filled with potassium vapor. Atoms that are resonant

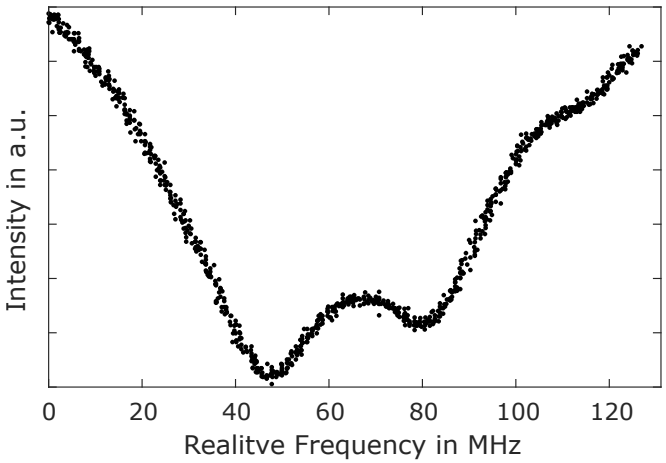



Figure B.4: **Doppler-free Absorption Spectrum of the Potassium D1-line.** The measured intensity shows the broad Doppler valley, extending beyond the figure, along with significantly sharper Doppler-free peaks.

with the laser will absorb the light. For a slightly detuned laser, only atoms width a velocity component along the laser propagation direction are resonant, due to the Doppler shift. The light is then retroreflected and passes through the cell again, meaning it is now resonant with atoms having the exact opposite velocity component. For a non-detuned laser, this implies that atoms with zero velocity component have the highest saturation through the incoming beam, and the retroreflected beam will not be absorbed as much. This results in narrow peaks in the absorption signal, with a width determined by the natural linewidth of the transition, on top of a much broader Doppler-broadened absorption profile. In our setup, the potassium vapor is heated to approximately 70 °C, which leads to a Doppler-broadened linewidth of about 800 MHz (FWHM).

A $\lambda/4$ wave plate placed before the cell is used to rotate the polarization of the retroreflected beam by 90° relative to the incoming beam, enabling separation of the two beams using a polarizing beam splitter. The absorption signal is then measured by a photodiode. The measured absorption spectrum is shown in Figure B.4. It displays the broad Doppler valley alongside significantly sharper Doppler-free peaks.

To obtain a clear absorption spectrum, the laser was locked to the Fabry–Pérot interferometer cavity, and the cavity length was scanned. This method was necessary as the laser's inherent stability of 40 MHz over 1 s was insufficient for a direct measurement. The signal from the photodiode after the cavity is effectively an error signal, which is then fed into a proportional-integral (PI) controller to generate the control signal required for stabilizing the seed laser. The wiring diagram for correctly processing the control signal for the slow and fast frequency modulation inputs is provided in Section B.6.

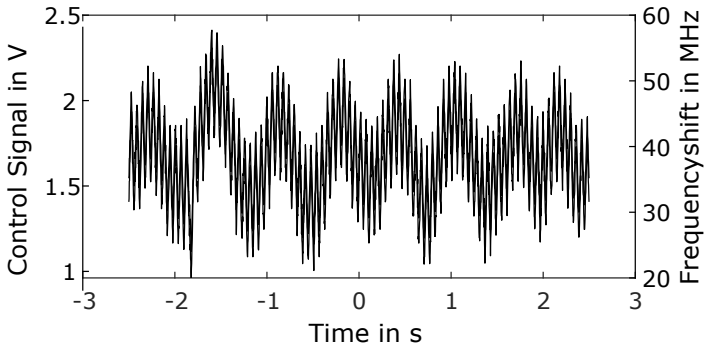



Figure B.5: **Control Signal of the Seed Laser Locked to the FPI Cavity.** The left y-axis shows the corresponding frequency shift of the control signal. The frequency has a standard deviation of 34 MHz on a time scale of 1 s.

Figure B.5 shows the control signal generated while the laser is locked to the rising edge of the intensity inside the FPI cavity, rather than an atomic transition. This characterization allows us to assess the frequency stability. With only the fast FM input connected, the frequency was stabilized to better than 0.1 MHz. The left y-axis displays the frequency shift, calculated using the sensitivity of 25 MHz $V^{-1}$ between the control signal and the frequency correction. The control signal oscillates around approximately 1.7 V, with a standard deviation of 34 Hz, which is in line with the manufacturer's specified stability (a deviation of 40 MHz over 1 s).

The control signal clearly contains two distinct frequency components: 20 Hz and 1.8 Hz. Both of these components disappear when the slow FM input is disconnected. The 20 Hz oscillation appears to result from a malfunction in the laser, which is currently under investigation by the manufacturer. The 1.8 Hz oscillation is caused by the PI controller values being optimized for the fast FM input only. In addition to these unwanted oscillations, the slow thermal FM does not perform as advertised: a linear input signal does not produce a consistent frequency shift, rendering it unreliable for laser cooling applications.

To lock the laser precisely onto the resonance (i.e., the maximum of the Doppler-free peak), the derivative of the absorption signal, known as the error signal, is needed. A coil surrounding the vapor cell generates a small alternating magnetic field, slightly shifting the energy of the $2S_{1/2}$ and $2P_{1/2}$ states. Using a lock-in amplifier, the error signal can be generated and then used as input for the PI controller to produce the control signal required for stabilizing the seed laser. Unfortunately, the inherent stability and the range of the laser's fast frequency modulation are insufficient to generate the error signal without first locking the laser to the FPI cavity. Therefore, a second PI controller would be needed to lock the laser frequency to the atomic transition. This step has not yet been achieved.

## B.4 Current Status and Outlook

In conclusion, the new laser setup meets the desired requirements for stable output power and polarization. However, a more reliable frequency modulation range is needed, and the frequency stability must be improved beyond the current 40 MHz over 1 s to be suitable for use in the experiment. The fiber-based seed laser and EDFA configuration allow for easy replacement of the seed laser with a model that offers better modulation capabilities and improved stability without any changes to the rest of the setup. This is a promising direction to achieve more stable laser, even tailored to our needs.

## B.5 List of Components for Laser Setup

All Components are available at THORLABS.

### Optical Components

- Lens Mount: LMR1/M
- Lens Tube: SM1L10
- Kinematic Mirror Mount: KM200
- Rotation Mount: RSP05/M
- Slip Ring: SM1RC/M
- Polarizing Beamsplitter: PBS054
- Beam Sampler: BSF10-C
- Mirror: BB111-E04
- Lens: LB1437-C-ML
- Lens: LB1056-C-ML
- $\lambda/2$ Plate: WPHSM05-1550
- Dichroic Mirror: DMLP950
- Achromatic Lens: ACA254-150-B

### Fabry-Pérot Interferometer

- Interferometer: SA200-12B
- Controller: SA201B

### Outcoupler

- Cage Mount: CP33B
- Cage Rod: ER2-P4
- Fiber Adapter Plate: SM1FCA2
- Aspheric Lens: AL1210M-C
- Cage Plate: CP33/M
- Cage Plate: CP32/M

### Fiber Components

- Fiber-to-Fiber Coupler: ADAFCPMB2
- Isolator: IOT-G-1550A

### Posts and Breadboard

- Breadboard: MB4560/M
- Post: RS075P4M
- Post: RS1.5P4M
- Post: RS1P4M
- Post: RS2P4M
- Post Spacer: RS1M
- Post Spacer: RS3M
- Post Spacer: RS4M
- Clamping Fork: CF125C/M-P5

## B.6 Wiring Diagram for Laser Setup

As mentioned in Section B.1, the seed laser has two possible frequency modulation options: the fast piezo and the slow thermal modulation. For both options, the input range is 0 V to 3 V. In order to use the same control signal from the PI-Controller, the steering signal from the PI-Controller is split into slow and fast components using a high-pass and low-pass filter. For the fast signal, an additional 1.5 V DC offset is added to keep the control signal in the middle of its range. The cutoff frequencies are 10 Hz for the low-pass and 1 Hz for the high-pass. After the low/high-pass filter, a unity gain buffer is connected to isolate the signal source from the load. For the slow thermal input, the control signal must also be flipped around 1.5 V, i.e. 0 V→3 V and 3 V→0 V, because the slow and fast inputs are shifting the frequency in opposite directions. For that, a differential amplifier with an attenuation of $6.8/330 \approx 0.021$ is used. With this amplification, it is possible to add a variable DC offset between 0 V and 3 V to tune the laser frequency manually over a wide frequency range. This is implemented using a potentiometer and a non-inverting amplifier, with an amplification of 1. The schematic wiring diagram is shown in Figure B.6.

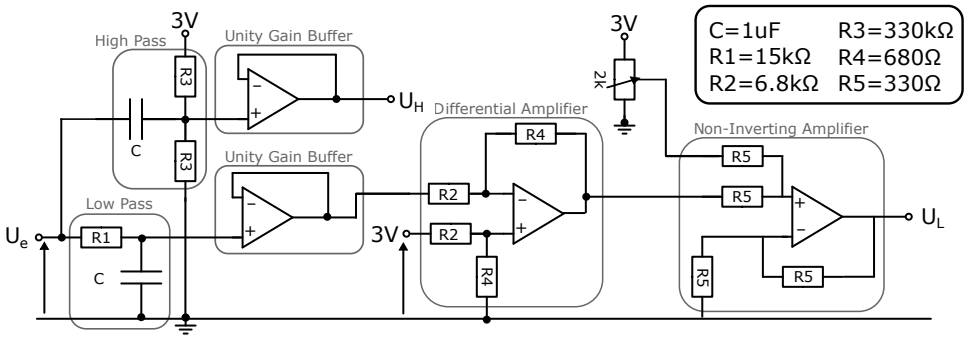



Figure B.6: **Wiring Diagram for Control Signal Processing.** The control signal from the PI-controller is split into high- and low-frequency components for the slow and fast frequency modulation inputs of the seed laser. With the second resistor in the high pass a 1.5 V offset is added to the fast signal. The slow signal is attenuated by approximately 0.021, inverted around 1.5 V, and a manual DC offset between 0 V and 3 V can be added.

## B.7 Python Script for Communication with Seed Laser

The seed laser can be controlled using the command line interface (CLI) and graphical user interface (GUI) provided by Pure Photonics. Unfortunately, it only works on Windows 8 or older. Therefore, a Python script which directly modifies values in the laser's registry via RS232 is presented here. The program can be used similarly to the CLI from Pure Photonics, as the commands are named identically. The full list of commands can be found on the website [46] in the 'Feature Guide'.

```
import serial
import time

# Define the serial port parameters
ser = serial.Serial('COM3', baudrate=9600, timeout=1)

def calcBIP4(data):
    bip8 = (data[0] & 0x0F) ^ data[1] ^ data[2] ^ data[3]
    bip4 = ((bip8 & 0xF0) >> 4) ^ (bip8 & 0x0F)
    return bip4

# Function to send a command and receive the response
def send_command(target_register, value,write):

    print(f"send_command({target_register}, {value},{write})")

    # Construct the packet
    if write:
        packet = [
        (calcBIP4([0x01,target_register, ((value >> 8) & 0xFF), (value & 0xFF), 0x00]) << 4) | 0x01,  #0x00 for read, 0x01 for write
        target_register,
        ((value >> 8) & 0xFF),  # Upper b yte of the value
        (value & 0xFF),  # Lower byte of the value
        ]
    else:
        packet = [
        (calcBIP4([0x00,target_register, ((value >> 8) & 0xFF), (value & 0xFF), 0x00]) << 4) | 0x00,  #0x00 for read, 0x01 for write
        target_register,
        ((value >> 8) & 0xFF),  # Upper byte of the value
        (value & 0xFF),  # Lower byte of the value
        ]

    # For Debbuging
    #print('send')
    #print(target_register, value)
    #for i in packet:
    #    print(i)
    # Send the packet

    try:
```

```
41          ser.write(bytes(packet))
42      except Exception as e:
43          print(f"Error during write: {e}")
44
45      time.sleep(0.1)
46
47      # Wait for the response
48      response = ser.read(4)
49
50      return response
51
52
53  def resena(x=0):
54      if x == 0 or x==1:
55          if x==0:
56              print(send_command(0x32, 0, True))
57          if x==1:
58              print(send_command(0x32, 8, True))
59      else:
60          print('value 0 or 1')
61
62  def pwr(x=None):
63      if x == None:
64          print(send_command(0xf8, 0,False))
65      else:
66          if x<1301 and x>599:
67              print(send_command(0xf8, x,True))
68          else:
69              print('value between 600 and 1300')
70
71  def cleanMode(x=0):
72      if x==0 or x==1 or x==2:
73          print(send_command(0x90, x, True))
74      else:
75          print('value 0,1 or 2')
76
77  def fcf(x=None):
78      if x == None:
79          print(send_command(0x35, 0, False))
80      else:
81          if x<195 and x>193:
82              i, d = divmod(x, 1)
83              ii = (send_command(0x35, int(i), True))
84              dd = (send_command(0x36, int(d*1000), True))
```

```
85              print(ii+dd/1000)
86          else:
87              print('value between 193 and 195')
88
89  def lf():
90      i=(send_command(0x40, 0, False))
91      d=(send_command(0x41, 0, False))
92      print(i+d/1000)
93
94  def ftf(x=None):
95      if x== None:
96          print(send_command(0x62, 0, False))
97      else:
98          print(send_command(0x62, x, True))
99
100 def slowinput(x):
101     if x>=0:
102         print(send_command(0xf8, x,True))
103     else:
104         print('positiv value please')
105
106 def cleanSweep(Start, End, n, resting=4):
107     for i in range(n):
108         print(print(send_command(0x62, Start, True)))
109         time.sleep(resting)
110         print(print(send_command(0x62, End, True)))
111         time.sleep(resting)
112
113 def oop():
114     print(send_command(0x42, 0, False))
115
116 def currents():
117     print(send_command(0x57, 0, False))
118
119 def temps():
120     print(send_command(0x58, 0, False))
121
122 def value_from_response(response):
123     upper_byte, lower_byte = response[2:4]
124     return (upper_byte << 8) | lower_byte
125
126 #def disconnect():
127 #    ser.close()
128
```

```
129 #def connect(com,btrate=9600,to=1):
130 #    ser = serial.Serial('COM'+str(com), baudrate=btrate, timeout
        =to)
131
132 while True:
133     user_input = input("Enter command (e.g., ftf(100)) or 'exit'
            to quit: ")
134
135     if user_input.lower() == 'exit':
136         break
137
138     try:
139         exec(user_input)
140     except Exception as e:
141         print(f"Error: {e}")
142
143 # Close the serial port
144 ser.close()
```

# Acknowledgments

On this final page of my thesis, I want to thank the people who made it all possible.

First, I'd like to thank Prof. Dr. Markus Oberthaler for giving me the chance to work on such an interesting and joyful topic for my master's thesis. I also want to thank Prof. Dr. Lauriane Chomaz for being my second examiner and for showing interest in my work.

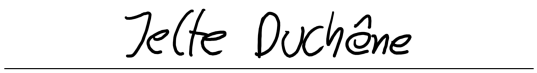
A huge thank you to the entire Matterwave Group for a warm welcome, for the great Friday breakfasts, the lunch times, and the other out-of-work activities.
I want to thank Dr. Helmut Strobel, who always made time for me whenever I needed help or advice, especially in the lab.
Special thanks also go to the BECK team for supporting me throughout the thesis and for the amazing time in the office and lab.
I'd also like to thank the mechanics workshop, especially Julia and David, for turning my messy sketches into precise custom parts.

I thank my girlfriend, Sophia, for the great times, for putting up with me when I was stressed, and for keeping my mind occupied with things other than physics.
And last but definitely not least, I thank my family—Merle, Bruno, and Regina—for always being there for me, supporting me throughout my studies, and always having a listening ear.

# Eigenständigkeitserklärung

Ich versichere, dass ich diese Arbeit selbstständig verfasst habe und keine anderen als die angegebenen Quellen und Hilfsmittel benutzt habe.

Heidelberg, den 4. Dezember 2024



Jelte Jan Luca Duchêne